





Cite this: *Chem. Soc. Rev.*, 2018, 47, 3217

Spotting the differences in two-dimensional materials – the Raman scattering perspective

Shishu Zhang,^a Na Zhang,^a Yan Zhao,^{ab} Ting Cheng,^{ab} Xiaobo Li,^{ac} Rui Feng,^{ab} Hua Xu,^c Zhirong Liu,^a Jin Zhang ^{*a} and Lianming Tong ^{*a}

Two-dimensional (2D) layered materials have attracted tremendous attention and led to a prosperous development in both fundamental investigation and device applications in various fields, such as nanoelectronics, flexible devices, sustainable energy and catalysts. The precise characterization of the structure and properties of 2D materials is in urgent need. Raman scattering spectroscopy is one of the most popular characterization tools that is convenient, rapid and non-invasive. It provides information on both the lattice structure from the frequency of phonon modes and the electronic band structure through the intensity due to electronic resonance Raman scattering. Although a few morphological characterization tools can image 2D materials with atomic resolution, Raman scattering measurements are more tolerant to the conditions of sample preparation such as the substrate and less technically demanding, and have been one of the routine tools for the characterization of 2D materials. In this review, we focus on the characterization of 2D materials using Raman scattering spectroscopy, in particular, the revealing of differences from primitive 2D materials, such as defects, doping effects, van der Waals heterostructures and the interaction with molecules. The characteristic Raman features of such differences and the corresponding interpretation will be discussed. We hope that this review will be useful for wide research communities of materials, physics, chemistry and engineering.

Received 15th December 2017

DOI: 10.1039/c7cs00874k

rsc.li/chem-soc-rev

1. Introduction

Two-dimensional (2D) materials have attracted broad interest since the discovery of graphene in 2004.¹ Owing to the layered structure with an atomic thickness, 2D materials exhibit superior optical,² electrical,³ thermal and mechanical properties,^{4–6} which are tunable by external conditions and have shown great potential in many fields such as nanoelectronics, flexible and wearable devices, sustainable energy and catalysts.^{7–10} Numerous 2D materials have been discovered in the last decade either by

^a Center for Nanochemistry, Beijing Science and Engineering Center for Nanocarbons, Beijing National Laboratory for Molecular Sciences, College of Chemistry and Molecular Engineering, Peking University, Beijing 100871, P. R. China. E-mail: jinzhang@pku.edu.cn, tonglm@pku.edu.cn

^b Academy for Advanced Interdisciplinary Studies, Peking University, Beijing, 100871, P. R. China

^c School of Materials Science and Engineering, Shaanxi Normal University, Xi'an, 710062, P. R. China



Shishu Zhang

Shishu Zhang is now a PhD student supervised by Prof. Jin Zhang in Center for Nanochemistry, College of Chemistry and Molecular Engineering at Peking University. She received her BS degree (2015) in Chemistry from Shandong University. Her current research interest focuses on the optical properties of two-dimensional materials.



Na Zhang

Na Zhang received her BS from Peking University in 2014. Since then, she joined Prof. Jin Zhang's group as a PhD student in the College of Chemistry and Molecular Engineering, Peking University. Her current research is focused on the Raman enhancement effect on two-dimensional layered materials.

mechanical exfoliation or chemical approaches, including insulators (such as hexagonal boron nitride (h-BN)),^{11,12} semiconductors (MoS₂, black phosphorus, *etc.*),^{13,14} semi-metal (such as MoTe₂)^{15,16} and topological insulators (Bi₂Se₃, Sb₂Te₃, *etc.*).¹⁷ Graphene consists of sp²-hybridized carbon atoms.¹ Owing to its high carrier mobility up to 10⁵ cm² V⁻¹ s⁻¹ and near-ballistic transport, graphene has been considered as a popular material in nanoelectronic applications.¹⁸ MoS₂ is a semiconducting material with a change of the indirect to direct bandgap (1.8 eV) from bulk to monolayer,¹³ and significant valley-spin coupling due to the broken inversion symmetry indicates its potential applications in spin electronic and valley electronic devices.^{19–21} The discovery of black phosphorus (BP) bridges the energy band gap between graphene (zero bandgap) and transition metal dichalcogenides (wide bandgap) with a tunable bandgap from 0.3 eV to 2.0 eV.²² One of the special characteristics of BP is the in-plane asymmetric structure, leading to anisotropic electrical, optical, and mechanical properties, such as anisotropic carrier mobility, photoluminescence, and Young's modulus.^{23–26} Held together by van der Waals forces, stacking heterostructures can also be assembled by two different layered materials.^{27,28} The charge redistribution at the interface and a possible change of the crystal structure induced by the neighboring materials and their relative orientation may provide more freedom of degree to modulate the optical and electrical properties of the materials and lead to more fascinating physical phenomena.^{29–31}

Raman spectroscopy is rapid, non-destructive and can provide both structural and electronic information of materials, and has been one of the most important tools for the characterization of 2D materials.^{32,33} The frequency, intensity, line-shape and full width at half maxima (FWHM) of Raman peaks can be directly related to the layer number, stacking order, defects, edges and crystalline orientation of the materials. Taking graphene as an example, the line-shape of the 2D Raman band (second-order resonance Raman scattering) and the relative intensity with respect to the G band have been widely used to identify the

layer number.³⁴ The defect-induced D band and D' band can indicate the density and environment (types) of defects.^{35,36} The G band blueshifts with either n-doping or p-doping owing to the non-adiabatic removal of the Kohn anomaly from the Γ point, while the 2D band redshifts with n-doping and blueshifts with p-doping due to the shift of the Fermi-level.³⁷ Furthermore, by improving the resolution by tip-enhanced Raman scattering, the grain boundary of CVD grown graphene can be clearly observed.³⁸

There exist several excellent reviews on the Raman scattering of 2D materials focusing on the Raman scattering process and phonon characteristics. Ferrari *et al.*³² demonstrated the basic physics of Raman scattering in graphene, and discussed the effects of edges, layers, defects and disorders, and perturbations. Wu *et al.*³⁹ presented a systemic review of the Raman spectroscopy of graphene based on its fundamental properties and application in devices. Zhang *et al.*⁴⁰ introduced many types of layered materials including semiconductors, topological insulators, superconductors, semi-metals and insulators. Lu *et al.*⁴¹ reviewed the Raman scattering features of 2D materials beyond graphene both in theoretical calculations and experimental investigations. In this review, we focus on the Raman spectroscopic characterization of 2D materials, in particular, the Raman features of materials with differences in the structure, such as defects, doping and stacking orders. The characterization of emerging materials in recent years, such as anisotropic black phosphorus and the van der Waals heterostructure, is also discussed. Meanwhile, the characterization of 2D materials using tip-enhanced Raman scattering (TERS) and the charge interaction between 2D materials and molecules are also discussed. Scheme 1 illustrates the typical structural differences in 2D materials and the corresponding representative Raman scattering characteristics that can be used to identify the structural differences.

This review article is organized as follows: in Section 2, the principle of the Raman scattering in 2D materials is discussed, particularly in graphene, h-BN and TMDs; Section 3 deals with the polarized Raman scattering features in emerging



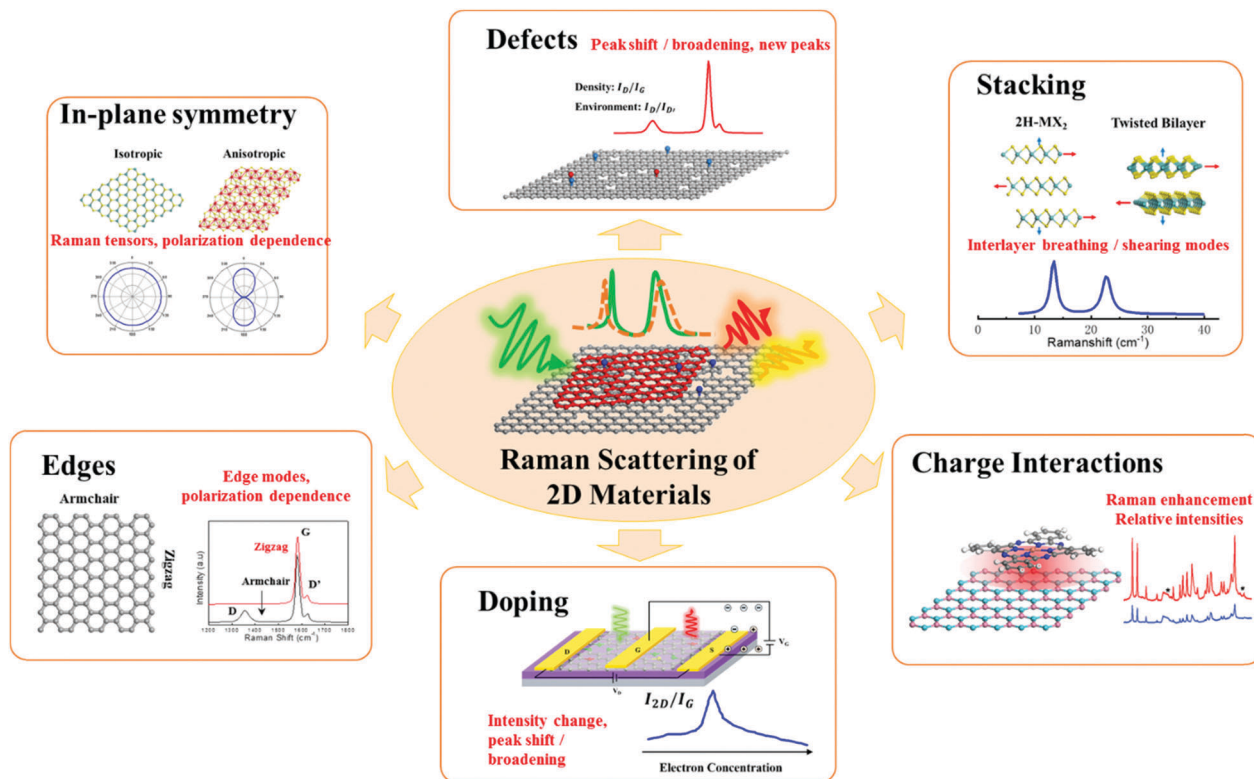
Jin Zhang

Jin Zhang was appointed as Changjiang Professor at Peking University, China, in 2013. He received his PhD degree in chemistry from Lanzhou University, China, in 1997. After a postdoctoral fellowship at the University of Leeds, UK, he returned to Peking University, where he was appointed as an associate professor in 2000 and promoted to a full professor in 2006. He is a fellow of the Royal Society of Chemistry. His research focuses on the controlled synthesis and spectroscopic characterization of carbon nanomaterials.



Lianming Tong

Lianming Tong received his BS and PhD degrees in chemistry from Peking University, China, in 2002 and 2007, respectively. He was an associate professor at Institute of Physics, Chinese Academy of Sciences, from 2011 to 2015. He is now an associate professor at College of Chemistry and Molecular Engineering, Peking University. His research interest includes Raman spectroscopy of low-dimensional materials and surface-enhanced Raman spectroscopy (SERS).



Scheme 1 Raman spectroscopic characterization of "differences" in 2D materials.

anisotropic materials; Sections 4 and 5 discuss the Raman spectroscopic characterization of defects and doping, and stacking orders, respectively; in Section 6, the TERS characterization of 2D materials is discussed; Section 7 mainly discusses the interaction between 2D materials and molecules probed by Raman enhancement; the Summary and outlook are given in the last section.

2. Principle of Raman scattering in 2D materials

For crystals, the energy of the lattice vibration generally ranges from tens to thousands of wavenumbers. In general, for visible light excitation, the photon energy is larger than that of the phonon by three orders of magnitude, and no direct coupling between the photon and phonon can occur.⁴² Instead, they should indirectly couple through the electron–phonon interactions. The Raman scattering process is basically composed of three parts: (1) an electron at the \mathbf{k} state absorbs an incident photon from the laser, then transits from the valence band to the conduction band; (2) the \mathbf{k} electron is inelastically scattered by a phonon \mathbf{q} in crystals to an intermediate state; (3) the \mathbf{k} electron returns to the valence band, recombining with a hole and a photon is released. The energy of the released photon can reduce (Stokes process) or increase (anti-Stokes process), resulting in different Raman peaks. The whole processes obey the energy and momentum conservation. Since the momentum changes of incident light and scattered light can be neglected, the

participation of a single phonon must satisfy its wavevector $\mathbf{q} \approx 0$ (Γ point in crystals), which is called the first-order Raman scattering process. The phonons of non-zero wavevector \mathbf{q} can also be observed in the Raman spectra, in which case at least two or more scattering processes are required. For example, a second-order Raman scattering process needs two phonons possessing equal and opposite momentum. The intensity of the high-order Raman scattering process is much weaker than that of the first-order process owing to the lower probability of high-order Raman scattering. However, if the energy of incident light equals to the energy required for an electronic transition, *i.e.*, the final state of the electron in the first scattering process is a real electronic state, the Raman cross-section will have a strong enhancement due to the resonance effect. This may make high-order processes stronger than first-order scattering, such as double resonance (DR) and triple resonance (TR), which have all been observed in 2D materials such as graphene and TMDs.^{33,43–47}

Fig. 1(a) shows the atomic structures of monolayer graphene, 2H-MX₂ (X = S, Se, Te) and ReX₂ (X = S, Se). 2H-MX₂ and graphene have a similar hexagonal structure from the top view, but actually 2H-MX₂ has three atomic layers as XMX. 1T'-ReX₂ is less symmetric, belonging to triclinic crystal system. These layers can commonly stack in a Bernal configuration (ABA) to form a few layers or bulk crystals.^{33,48} Both ABA stacked graphene and 2H-MX₂ have D_{6h} point group symmetry with 4 and 6 atoms in their unit cells, respectively, resulting in 12 and 18 phonon modes, three of which are acoustic. For ReX₂,

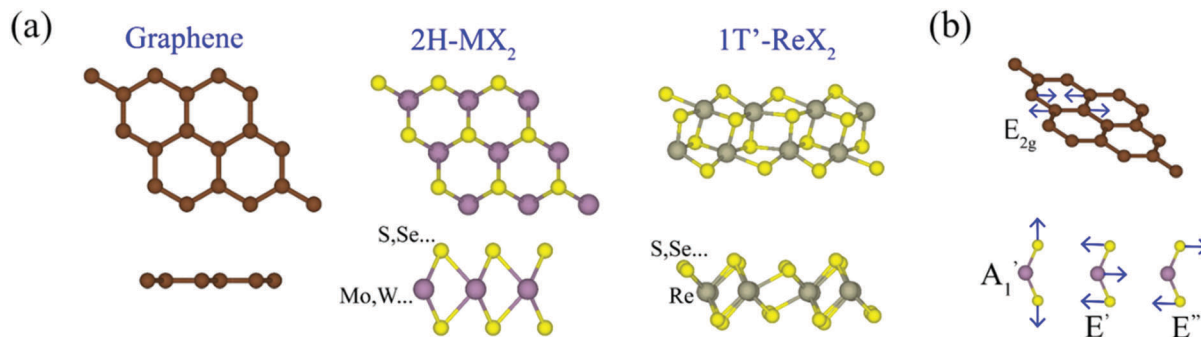


Fig. 1 (a) Atomic structures of monolayer graphene, 2H-MX₂ and 1T'-ReX₂, viewed from top and side. (b) First-order Raman-active atomic vibrational modes in monolayer graphene and 2H-MX₂.

bulk ReX₂ has 12 atoms in a unit cell and thus possesses 33 optical and 3 acoustic modes. In the case of a monolayer, graphene still belongs to D_{6h} but 2H-MX₂ reduces to point group D_{3h} owing to the missing of inversion symmetry operation. ReX₂ still has C_i symmetry similar to the bulk.

According to the point group of the crystals and numbers of atoms in the primitive cell, one could obtain the first-order lattice vibration modes at the Γ point. Group analysis helps to specify which representations are acoustic modes, Raman or IR active optical modes. For monolayer graphene with D_{6h} point group symmetry and two atoms in a unit cell, phonons at the Γ -point can be $A_{2u} + E_{1u} + B_{2g} + E_{2g}$, where A_{2u} and E_{1u} are acoustic modes, B_{2g} is optically inactive and only E_{2g} is Raman active. A monolayer 2H-MX₂ with D_{3h} point group symmetry and three atoms in a unit cell has 9 vibration modes, which are expressed as: $\Gamma = 2A_2'' + A_1' + 2E' + E''$, where "E" denotes double degenerate modes in the x - y plane. Among these modes, only one A_2'' and one E' belong to acoustic modes, another A_2'' is IR active and E' is both Raman and IR active. Both A_1' and E'' are Raman active. For ReX₂, 36 normal vibration modes are represented by $\Gamma = 18A_g + 18A_u$, with 18

Raman active A_g modes. Fig. 1(b) shows the first-order Raman active vibration modes in monolayer graphene and 2H-MX₂. It can be found that the E'' mode in 2H-MX₂ is somewhat similar to the E_{2g} mode in graphene. They both represent adjacent atoms vibrating in the opposite phase in the x - y plane.

The calculated phonon dispersions of typical 2D materials, that are monolayer (1L) graphene, h-BN and MoS₂, are depicted in Fig. 2(a-c).⁴⁹ The vibration modes are marked with the corresponding irreducible representations at the Γ point. Three acoustic branches are composed of two in-plane modes: the longitudinal acoustic (LA) and the transverse acoustic (TA) modes, and one out-of-plane acoustic (ZA) mode. Their frequencies are all zero at the Γ point which represent the overall translations along three directions of crystals. For optical branches, graphene has two in-plane (E_{2g}) optical and one out-of-plane (B_{2g}) modes, and h-BN also has three optical modes including the double degenerate E_{2g} and nondegenerate B_{2g} modes.⁵⁰ 2H-MoS₂ has four in-plane optical modes composed of E'' (LO_1 , TO_1) and E' (LO_2 , TO_2) modes and two out-of-plane optical modes (A_1' , A_2''). The above-mentioned double degenerate E mode behaves here as the degenerate LO branch and TO branch. ReS₂ has more optical

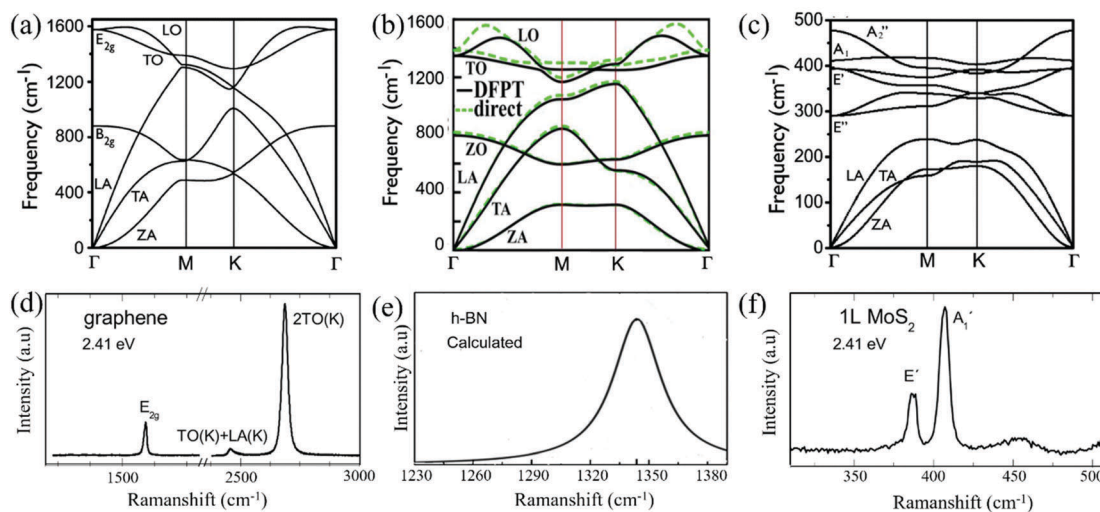


Fig. 2 (a-c) Calculated phonon dispersion of one-layer graphene (a), h-BN (b) and 2H-MoS₂ (c). (d-f) Typical Raman spectrum of one-layer graphene (d), h-BN (e) and 2H-MoS₂ (f). Adapted with permission from ref. 49, 50 and 52. Copyright 2014, ACS Publications, 2009, APS Physics, and 2017, RSC Publishing.

branches owing to more atoms in its primitive cell. The phonon dispersion curves of such bulk crystals are nearly similar to the layered materials resulting from the weak van der Waals interactions between each layer, and they have more new branches owing to the increase in the number of atoms which are not shown here.^{33,51}

Fig. 2(d–f) shows the typical Raman spectra of 1L graphene, h-BN and MoS₂.⁴⁹ For graphene, the G peak is the first-order Raman mode E_{2g}, but the G' (2D) peak belongs to the second-order vibrational mode.³³ As the structure analogue of graphene, h-BN shows different Raman spectra from those of graphene. Only a Raman G band corresponding to the E_{2g} vibration mode is detected but no D band due to the lack of Kohn anomaly.^{50,52} For the first-order vibration modes in MoS₂, only E' and A₁' can be observed, and E'' modes are forbidden under backscattering geometry.⁵³ The Raman spectra of bulk and few-layer ReS₂ have 18 A_g modes.⁵⁴ Its anisotropic feature also makes its Raman spectrum depend on the polarization of incident laser and the crystal orientation, which will be described in detail in the next section.

The high-order Raman modes of graphene and MoS₂ have also been well-studied.^{33,43,44,46,47} Malard *et al.* have summarized the origin of common peaks in graphene [see Fig. 3].³³ The second-order Raman scattering requires two processes. For the D-band, it is considered that the electron at the K point is first scattered by defects of crystals elastically and then inelastically scattered with the TO phonon at the K' point. For the D'-band, the two processes consist of one scattering event by defects and another by the LO phonon. The G' peak is related to two inelastic scattering processes between the electron and the TO phonon. Both the G' peak and D peak are due to inter-valley double-resonance scattering processes but the D' peak is due to an intra-valley process. Electrons can not only be scattered by phonons, but also scattered by holes, resulting in a triple-resonance Raman scattering process in graphene. In the case of MoS₂, the most common second-order peak is around 450 cm⁻¹, which is attributed to 2LA phonons at the M point.⁵⁵ Golasa *et al.* have observed multiphonon resonant Raman scattering in MoS₂,

and assigned the peaks to both A (basic first-order modes such as E' and A₁' modes) and XA (LA, TA and ZA) phonon replicas of vibrational modes from the high-symmetry M point of the Brillouin zone.⁴³ Sun *et al.* also have studied the triple resonant Raman peak in MoS₂, which was correlated with spin-orbit splitting in single-layer MoS₂.⁵⁶ In addition, the high-order peak G' of graphene is generally much stronger than the first-order G peak, due to its higher-order resonance.³³ The frequency of the G' mode is linearly dispersive with the excitation energy due to Kohn anomaly at K-TO.^{57,58} MoS₂ belongs to a direct-gap semiconductor, and its absorption spectrum has two obvious excitation absorption peaks (A, B), resulting in the emergence of lots of new resonant peaks and the Raman spectra strongly depend on the laser excitation energy.¹³ Recently, the resonant Raman spectra of ReS₂ have also been reported.⁵⁹

For the few-layer graphene and TMDs, the Raman scattering process is affected by the interlayer coupling.^{33,49} For example, the first-order Raman-active peaks shift with the number of layers and extra interlayer vibration modes appear at low (< 50 cm⁻¹) frequencies, that is, shear modes and breathing modes.^{60,61} These are due to the interlayer van der Waals interactions and the long-range Coulomb forces in layered materials.⁵¹ For ReS₂, the splitting of low-frequencies in ReS₂ was observed,⁶² and it was reported that there is almost no difference in Raman shifts between the bulk and the monolayer, which may suggest weak interlayer interactions in this material.⁵⁴

3. Identifying the in-plane anisotropy of 2D materials

Since black phosphorous has been rediscovered in 2014, the anisotropic 2D materials have been widely studied.¹⁴ Due to the reduced symmetry, the anisotropic materials exhibit unique electrical, optical and mechanical properties.^{63–66} Characterizing the in-plane anisotropic properties and identifying the crystalline orientation are important for further studies. Raman spectroscopy is a rapid and nondestructive method to characterize the

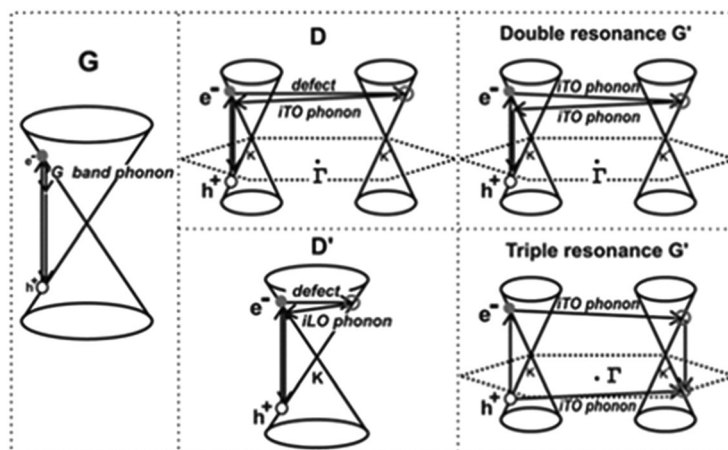


Fig. 3 Schemes of high-order resonances Raman scattering in graphene, reproduced with permission from ref. 33. Copyright 2009, Elsevier.

anisotropy of such materials, compared to the electrical measurement and transmission electron microscopy.^{67,68} Owing to the different forms of Raman tensors that are determined by the structural symmetry and vibrational symmetry, Raman modes show different polarization dependent intensities. As a result, polarized Raman spectroscopy has been a useful tool to identify the in-plane symmetry of 2D materials.^{62,63,67,69–72}

3.1 Raman selection rules

Polarized Raman spectroscopy is an effective method to characterize the symmetry of the crystal structure and the vibrational modes.⁷³ The detections of Raman-active modes are strongly dependent on the scattering geometry and symmetry. The selection rules for the Raman-active phonons can be obtained strictly by group theory, the intensity of a particular mode is proportional to $|e_s \cdot \hat{R} \cdot e_i|^2$, where e_i and e_s are the electric vectors of the incident and scattered light.⁷³ \hat{R} is a derivative of the polarizability tensor, usually called the Raman tensor, which is determined by the point group and the symmetry of the mode according to the group theory, expressed as

$$\begin{pmatrix} \alpha_{xx} & \alpha_{xy} & \alpha_{xz} \\ \alpha_{yx} & \alpha_{yy} & \alpha_{yz} \\ \alpha_{zx} & \alpha_{zy} & \alpha_{zz} \end{pmatrix}.$$

The intensity of the Raman-scattered light is then dependent on the directions of incident and analyzer polarization relative to the principal axes of the crystal.

Experimentally, the parallel or cross polarization configuration in polarized Raman spectroscopy is obtained by setting the polarization directions of the incident polarizer and the analyzer parallel or perpendicular. The z-direction is usually defined as the normal direction of the sample. Taking 2H-MoS₂ (*D*_{6h}) as an example, the Raman tensors of the Raman active phonons in the Brillouin center, that are A_{1g}, E_{1g}, and E_{2g} modes,⁷⁴ are presented as follows:

$$R(A_{1g}) = \begin{pmatrix} a & 0 & 0 \\ 0 & a & 0 \\ 0 & 0 & b \end{pmatrix}$$

$$R(E_{1g}) = \begin{pmatrix} 0 & 0 & 0 \\ 0 & 0 & c \\ 0 & c & 0 \end{pmatrix}, \begin{pmatrix} 0 & 0 & -c \\ 0 & 0 & 0 \\ -c & 0 & 0 \end{pmatrix}$$

$$R(E_{2g}) = \begin{pmatrix} 0 & d & 0 \\ d & 0 & 0 \\ 0 & 0 & 0 \end{pmatrix}, \begin{pmatrix} d & 0 & 0 \\ 0 & -d & 0 \\ 0 & 0 & 0 \end{pmatrix}$$

with backscattering geometry, E_{1g} modes are forbidden in both the parallel configuration (XX or YY) and the cross configuration (XY or YX), for the lack of the z-component of the incident polarization. For the A_{1g} mode ($\sim 408.6 \text{ cm}^{-1}$), in parallel configuration ($e_s = e_i = (1 \ 1 \ 0)$), $I(A_{1g}) = a^2$, while in the cross

configuration ($e_s = (0 \ 1 \ 0)$, $e_i = (1 \ 1 \ 0)$), $I(A_{1g}) = 0$. For E_{2g} modes ($\sim 32.5 \text{ cm}^{-1}$ and 383.3 cm^{-1}), in the parallel configuration and the cross configuration, $I(A_{1g}) = d^2$.⁷⁵ This indicates that polarized Raman spectroscopy is an effective method to assign the symmetry of Raman-active phonon modes.

By rotating the samples under fixed incident and scattered polarization, the Raman intensities could change periodically with the angle θ between the polarization direction and the principal crystal axes.^{68,73} The A_g modes of the orthorhombic 2D materials are taken as an example, the Raman tensor of which has the form as:

$$R(A_g) = \begin{pmatrix} a & 0 & 0 \\ 0 & b & 0 \\ 0 & 0 & c \end{pmatrix}$$

The Raman intensity in the parallel configuration can be expressed as

$$I(A_g) = \left| (\cos \theta \ \sin \theta) \cdot \begin{pmatrix} a & 0 & 0 \\ 0 & b & 0 \\ 0 & 0 & c \end{pmatrix} \cdot \begin{pmatrix} \cos \theta \\ \sin \theta \\ 0 \end{pmatrix} \right|^2$$

$$= (a \cos^2 \theta + b \sin^2 \theta)^2,$$

indicating a 180° periodic variation with θ , which reaches maximum or minimum when the crystalline orientation is parallel to the incident and scattered polarization based on the Raman selection rules, the intensity variation can be strictly calculated, which provides a method for identifying the crystalline orientation in anisotropic 2D materials including orthorhombic, monoclinic and triclinic materials.^{63,68}

3.2 Identifying the crystalline orientation of anisotropic 2D materials

BP has a folded honeycomb structure with 4 atoms in a unit cell, which belongs to the orthorhombic crystal system (*D*_{2h},¹⁸ *Cmce*).⁶¹ There are 12 phonon modes in the Brillouin center:

$$\Gamma = 2A_g + B_{1g} + B_{2g} + 2B_{3g} + A_{1u} + 2B_{1u} + 2B_{2u} + B_{3u},$$

six of which are Raman-active modes, including A_g, B_{1g}, B_{2g}, and B_{3g}, but only the A_g and B_{2g} modes can be detected with backscattering geometry as shown in Fig. 4(a).⁶⁸ The Raman tensor of A_g and B_{2g} modes in black phosphorus can be expressed as follows:

$$R(A_g) = \begin{pmatrix} a & 0 & 0 \\ 0 & b & 0 \\ 0 & 0 & c \end{pmatrix} \quad R(B_{2g}) = \begin{pmatrix} 0 & 0 & e \\ 0 & 0 & 0 \\ e & 0 & 0 \end{pmatrix}$$

The angle-dependent Raman intensities are $I(A_g) = (a \cos^2 \theta + c \sin^2 \theta)^2$ and $I(B_{2g}) = e^2 \sin^2 2\theta$ in the parallel configuration. As shown in Fig. 4(b) and (f), the A_g modes have a 180° variation period and the maxima appear when the armchair or zigzag direction is parallel to the polarization direction. The B_{2g} mode

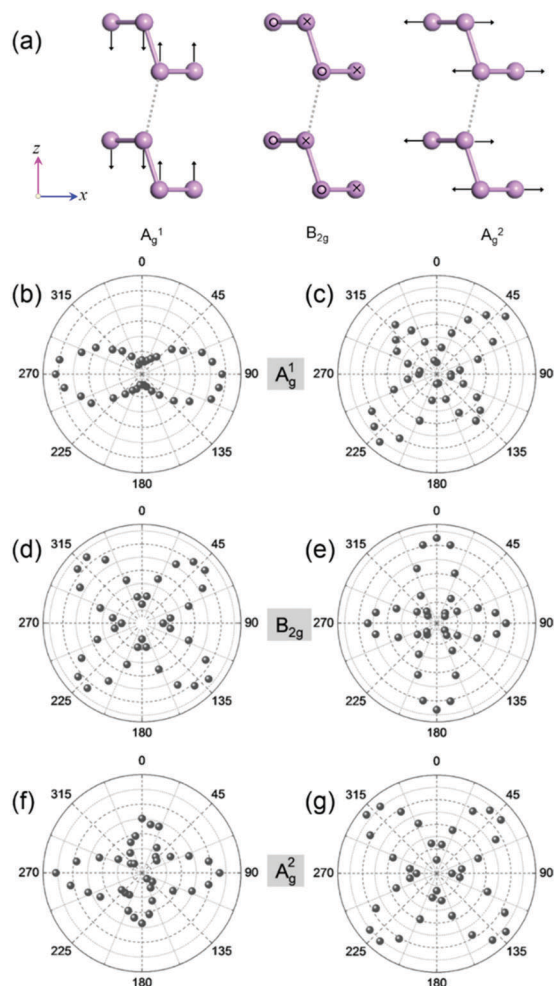


Fig. 4 (a) Atomic displacements for Raman-active modes in BP. (b) Polar plots of the fitted peak intensities of (b and c) A_g^1 , (d and e) B_{2g} , and (f and g) A_g^2 modes as a function of sample rotation angle θ in (b, d and f) parallel and (c, e and g) cross-polarization configurations on Si/SiO₂ substrates. Adapted with permission from ref. 68. Copyright 2015, Wiley.

has a 90° variation period and the maximum reaches when $\theta = 0$. In the cross configuration, $I(A_g) = (a - c)^2 \sin^2 2\theta/4$ and $I(B_{2g}) = e^2 \cos^2 2\theta$. Both A_g and B_{2g} modes have 90° variation periods. For the A_g modes, the directions of maximum intensities coincide with the armchair and zigzag directions. In comparison with electrical conductance measurements, the angular dependence of Raman intensities is then used to identify the crystalline orientation of BP.⁶⁸

It should be noted that BP exhibits anomalous polarization dependence.^{63,69,72,76,77} For A_g modes, except the maximum in the 180° variation period, a secondary maximum also exists in the parallel configuration, which does not agree with the Raman selection rules. The maximum intensity of the same mode is reached with the polarization being parallel to the armchair or zigzag direction decided by the excitation laser wavelength and sample thickness.^{63,69,76,77} There are two major interpretations for this phenomenon. One is the consideration of optical dichroism, which indicates a complex dielectric function with the imaginary part.⁷⁷ The Raman tensor is a derivation of

the dielectric tensor, so the forms of Raman tensor elements are also complex, which leads to the deviation of the classical Raman selection rules. The birefringence effect is another explanation of the anomalous phenomenon.⁶⁹ Owing to the anisotropic crystal structure, the refractive indices are different along armchair and zigzag directions. The polarization states of the incident and scattered light are altered when light propagates in BP. By introducing a phase delay factor due to the birefringence effect, the polarization dependence of Raman intensities can be well fitted. It has also been found that electron–photon and electron–phonon interactions are influenced by the sample thickness and excitation laser wavelength.⁶³ In addition, the interference effect on the Si/SiO₂ substrates between the interfaces should also be considered when discussing the polarization dependence of BP.⁷⁶

A family of group IV monochalcogenide layered materials, including SnS, SnSe, GeS and GeSe,^{64,78–80} has a similar crystal structure which belongs to the orthorhombic crystal system ($Pnma$, D_{2h}^{16}). There are 24 phonon modes at the center of the Brillouin zone:

$$\Gamma = 4A_g + 2B_{1g} + 4B_{2g} + 2B_{3g} + 2A_u + 4B_{1u} + 2B_{2u} + 4B_{3u},$$

where $4A_g$, $2B_{1g}$, $4B_{2g}$ and $2B_{3g}$ are Raman-active modes,⁸⁰ and show obvious polarization dependence identical to the Raman selection rules.

With the reduced crystal symmetry, 2D materials that belong to triclinic crystal including ReS₂ and ReSe₂ exhibit much more unique polarization dependent features.^{59,71,81,82} Different from other transition-metal dichalcogenides, ReX₂ (X = S and Se) has a stable 1T' phase instead of the 2H phase. Except the Re–X bonds, Re–Re bonds also exist in ReX₂ to constitute a Re₄ parallelogram and the zigzag chain of Re is defined as the b -axis.⁵⁴ Owing to the Re₄ structure, there are 12 atoms in the ReX₂ unit cell, and 36 phonon modes in the Brillouin zone center, including 18 A_g modes (Raman-active) and 18 A_u modes (15 infrared-active modes and 3 acoustical modes).⁵⁴ The Raman tensor of A_g modes can be expressed as

$$\begin{pmatrix} a & d & e \\ d & b & f \\ e & f & c \end{pmatrix},$$

with backscattering geometry,⁷³ all the A_g modes can be detected which exhibit polarization dependence in the parallel or cross configuration. The intensities mode V (212 cm⁻¹) of ReS₂ and mode V (162 cm⁻¹) of ReSe₂ reach the maximum when the b -axis (zigzag Re–Re chain) is parallel to the incident and scattered polarization with 532 nm excitation wavelength, so the crystalline orientation could be identified.^{62,71} The same as black phosphorus, ReS₂ also exhibits anomalous polarization dependence which is not coincident with the classical Raman selection rules owing to the anisotropic optical environment.⁸¹ The polar plots of the angle-resolved polarized Raman spectra of ReS₂ in the parallel configuration exhibit unique twisted butterfly patterns, leading to the failure of identifying the crystalline orientation with 632.8 nm excitation laser wavelength.

Notably, ReS₂ belongs to the C_i point group, which only has an inversion center but no C₂ symmetry axis, so it has two different vertical orientations in the 2D dimension including “upward” and “downward” orientations. The angle-resolved polarized Raman spectra and the circularly polarized Raman spectra can be used to identify the vertical orientation.⁸² With the “upward” orientation, the Raman tensor is

$$\begin{pmatrix} a & d & e \\ d & b & f \\ e & f & c \end{pmatrix},$$

while with “downward” orientation, a rotation of 180° about the *b*-axis changes the Raman tensor from

$$\begin{pmatrix} a & d & e \\ d & b & f \\ e & f & c \end{pmatrix} \text{ to } \begin{pmatrix} a & -d & -e \\ -d & b & f \\ -e & f & c \end{pmatrix}.$$

With a linearly polarized incident light and no analyzer, the Raman intensity is decided by the angle θ between the *b*-axis and incident polarization as $|\tilde{\chi} \cdot \hat{e}_i|^2$. With the “upward” orientation, the Raman intensity can be expressed as:

$$I \propto a^2 \cos^2 \theta + b^2 \sin^2 \theta + d^2 + 2d(a + b) \sin \theta \cos \theta.$$

With the “downward” orientation, the Raman intensity can be expressed as:

$$I \propto a^2 \cos^2 \theta + b^2 \sin^2 \theta + d^2 - 2d(a + b) \sin \theta \cos \theta.$$

The relative maximum angles of mode III (150 cm⁻¹), mode IV (160 cm⁻¹) and mode V (211 cm⁻¹) could be different with different vertical orientations under 532 nm excitation wavelength.

As for the circularly polarized Raman spectra, with right-handed or left-handed circularly polarized incident light being introduced, the ReS₂ flakes would have different Raman responses owing to the birefringence effect and optical dichroism.⁸¹ With different vertical orientations, for the same modes, the relative intensities under right-handed and left-handed circularly polarized incident light are opposite. With the “upward” orientation, the Raman intensities of modes I, II and V are much larger under 514.5 nm excitation by left-handed circularly polarized laser than by right-handed circularly polarized light, while with the “downward” orientation, the Raman intensities of modes I, II and V are much larger under 514.5 nm excitation by right-handed circularly polarized laser than by left-handed circularly polarized light. This phenomenon may also exist in other 2D materials which belong to a triclinic crystal system and using circularly polarized Raman spectra is a rapid and effective method to identify the vertical orientation.

For a monoclinic crystal structure, like GaTe, 1T' MoTe₂, and MS₃ (M = Ti, Zr, and Hf),^{15,67,83} the features of the polarized Raman spectra resemble the orthorhombic crystal system and can be analysed using the Raman section rules.

4. Identifying the defects and doping in 2D materials

The most straightforward and precise method to identify defects in 2D materials is atomically-resolved morphological characterization, for example, high-resolution transmission electron microscopy (HR-TEM) and scanning tunneling microscopy (STM). However, such characterization is limited to areas of tens of nanometers, and requires special sample preparation processes. Raman spectroscopy is highly sensitive to symmetry-breaking defects in materials, and can provide information on the defect type, density and distribution from much larger areas of samples.^{36,84–87} The atomic vacancies and hetero-atoms in the structure perturb the lattice vibration and lead to a peak shift, width broadening and the appearance of new peaks.

4.1 Identifying the defects in 2D materials

Defects in 2D materials are scattering centers in the second order Raman scattering process, where the scattering of an excited electron by a defect occurs with momentum conservation. Consequently, several peaks closely related to disorders appear in the Raman spectra, enabling the identification of defects in 2D materials through Raman spectroscopy.^{33,86}

Fig. 5(a) shows the Raman spectra of single layer graphene (SLG) on Si/SiO₂ substrates. The D band (~1350 cm⁻¹) and D' band (~1620 cm⁻¹) are characteristics of the existence of defects. They both originate from double resonance Raman processes, consisting of one elastic scattering event by defects and one inelastic scattering event by emitting or absorbing a phonon, respectively.^{33,88}

In the case of TMDs, there are two main second order Raman scattering processes, one related to two phonons within the interior of the Brillouin zone and the other to one phonon and a defect.⁴⁹ For MoS₂ and WS₂, the most prominent Raman bands related to defects are at around 223 cm⁻¹ and 172 cm⁻¹, respectively. These bands are assigned to longitudinal acoustic (LA) phonons at the *M* point and are called LA(*M*) bands.^{89,90} The effect of disorders in MoS₂ on the Raman modes is shown in Fig. 5(c). Both the widths and positions of the two first order Raman bands (E' and A1') change with the presence of defects, and new Raman scattering peaks appear in the spectral region 140–420 cm⁻¹.⁹¹ The evolution of the first order Raman peaks can be explained by a phonon confinement model,⁹² and the new peaks originate from the phonons at the edge of the Brillouin zone activated by the momentum contribution of a defect. For WSe₂, the most prominent band induced by disorders is at 263 cm⁻¹, which corresponds to a phonon belonging to the *A*-symmetry optic branch at the *M* point and is labelled as the A(*M*) band in the literature.⁹³ For MoSe₂, vacancies result in missing Mo–Se bonds and reduce overall restoring force, which consequently leads to the decrease of the frequency of the A_{1g} peak. The calculations show that when the vacancy concentration is relatively high (~25%), several new peaks appear at ~150 cm⁻¹, ~270 cm⁻¹, ~300 cm⁻¹ and ~350 cm⁻¹, which are likely related to defects, and the experimental results also confirm the defect-activated peaks.⁹⁴ However, the possible effect of defects on the Raman spectra of some 2D materials,

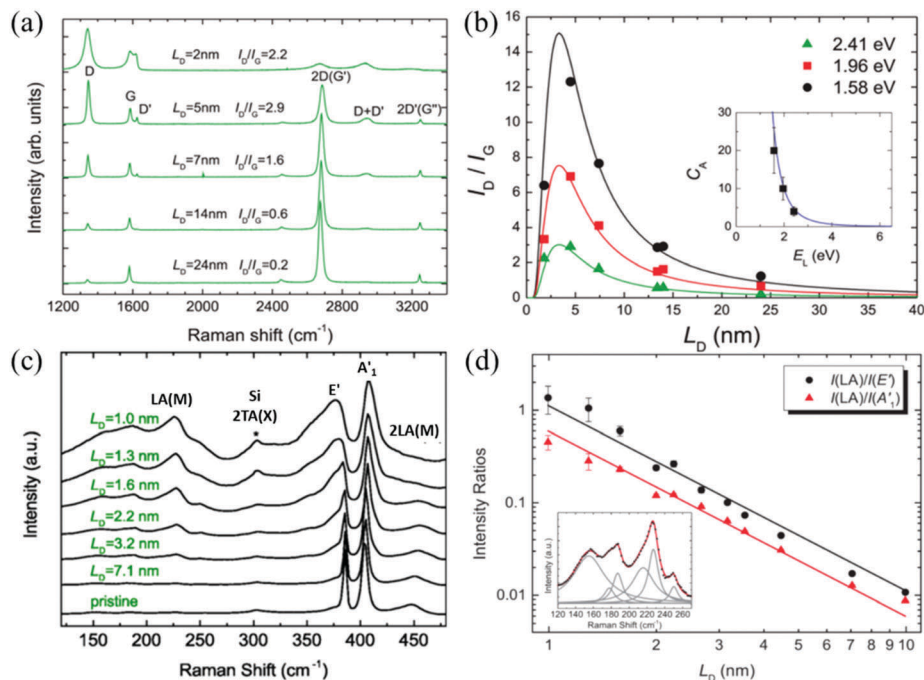


Fig. 5 (a) Raman spectra of five ion-bombarded single-layer graphene (SLGs) measured at $E_L = 2.41$ eV ($\lambda_L = 514.5$ nm) on Si/SiO₂ substrates. (b) I_D/I_G as a function of L_D using three lasers. The inset plots C_A as a function of E_L . The solid curve is given by $C_A = 160 E_L^{-4}$.³⁶ Adapted with permission from ref. 36. Copyright 2011, ACS Publications. (c) Raman spectra of 1L-MoS₂ flakes on Si/SiO₂ with varying L_D . The asterisk refers to the 2TA(X) Raman peak of the Si substrate. The spectra have been normalized to the intensity of the A₁' peak. (d) Experimental intensity ratio $I(LA)/I(E')$ and $I(LA)/I(A_1')$ of MoS₂. The solid lines are linear fits with slope equal to -2 . The low frequency bands, where the LA peak is located at ~ 227 cm⁻¹, are shown in the inset, along with the corresponding Lorentzian fits.⁹¹ Adapted with permission from ref. 91. Copyright 2015, APS Physics.

such as ReS₂, is still not well-studied yet and awaiting for further exploration.⁵⁹

The density of defects determines the quality of materials and its potential applications. From the Raman spectra, the intensities of the defect-induced peaks directly reflect the density of defects. For example, the intensities of D and D' bands of graphene increase with an increasing amount of defects at a relatively low density. Further increasing the density, the intensity of the D band decreases whereas the D' band remains unchanged. More importantly, as Fig. 5(b) shows, the intensity ratio of D to G bands (I_D/I_G) is correlated with the average distance between two point defects L_D . Besides, Fig. 5(b) shows that the intensity ratio is also related to the excitation energy E_L . The relation between L_D , I_D/I_G , and E_L is given by^{36,95}

$$L_D^2 (\text{nm}^2) = \frac{(4.3 \pm 1.3) \times 10^3}{E_L^4} \left(\frac{I_D}{I_G} \right)^{-1}$$

The defect density n_D can then be calculated by

$$n_D (\text{cm}^{-2}) = (7.3 \pm 2.2) \times 10^9 E_L^4 \left(\frac{I_D}{I_G} \right)$$

In the case of MoS₂, as shown in Fig. 5(d), the intensity ratio $I(LA)/I(E')$ and $I(LA)/I(A_1')$ is inversely proportional to the square of L_D following the equation⁹¹

$$\frac{I(LA)}{I(X)} = \frac{C(X)}{L_D^4}$$

where $X = E'$ or A_1' and $C(X)$ is constant, for example, $C(E') = 1.11 \pm 0.08$ nm², and $C(A_1') = 0.59 \pm 0.03$ nm². Thus the intensity ratio can also be used to quantify the density of defects within the lattice of MoS₂. This work provides a practical approach to identify the presence of disorders and to calculate the density of defects in single layer MoS₂ using Raman spectroscopy. The change of density of defects can also be monitored using the Raman spectra.

In the case of MoSe₂, the frequency of the A_{1g} peak can be used to evaluate the vacancy concentration. With the increasing Se vacancy concentration, the A_{1g} peak downshifts and there is a quasi-linear dependence between the A_{1g} peak frequency and the Se vacancy concentration, which allows the A_{1g} Raman mode to be a fingerprint of the vacancy concentration in monolayer MoSe₂, and may be extended to other TMD systems.⁹⁴

Various types of defects exist in 2D materials. In general, hetero-atoms in the crystal lattice, anomalous covalent bonding between atoms, terminal functional groups are the three major types of defects. Defects can appear during synthesis, sample treatment and even measurements. On the other hand, defects can also be introduced intentionally for the chemical functionalization of materials. For example, for graphene, vacancy-like defects can be produced by Ar ion bombardment and the sp³-hybridized carbon defects can be introduced by fluorination and mild oxidation.^{92,96} The corresponding D' bands of these two defects are different, as shown in Fig. 6(a). Fig. 6(b) shows that the intensity ratio of the D to D' band ($I_D/I_{D'}$) is closely related to the nature of defects. $I_D/I_{D'}$ is

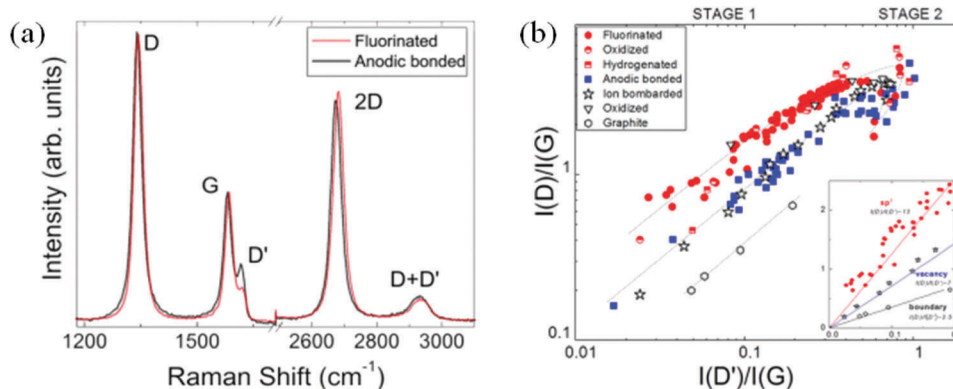


Fig. 6 (a) Raman spectra of fluorinated (red) and defective graphene produced by anodic bonding (black), showing the same D, G, and 2D intensities but different D' intensities. (b) $I_{\text{D}}/I_{\text{G}}$ versus ratio $I_{\text{D}'}/I_{\text{G}}$. The inset shows the linear dependence between the two parameters at a low defect concentration, giving different $I_{\text{D}}/I_{\text{D}'}$ for different types of defects. The graphene samples are exfoliated on Si/SiO₂. Adapted with permission from ref. 35. Copyright 2012, ACS Publications.

about 13 for sp³-hybridized carbon defects, while for vacancy-like defects, it decreases to 7, and for boundaries in graphene, it has a minimum of 3.5.³⁵ Besides, a recent study established a method to disentangle contributions of point-like and line-like defects to the Raman spectra of graphene-related materials.⁸⁵ From theoretical simulations, this work gave the relationship between $(A_{\text{D}}/A_{\text{G}})E_{\text{L}}^4$ and Γ_{G} with different densities of defects, where $(A_{\text{D}}/A_{\text{G}})$ is the ratio of peak areas of D and G bands, E_{L} is the excitation laser energy, and Γ_{G} is the G-band line width. Eventually a diagram to identify separately the contributions from each type of defects was given. These results make it possible to determine quantitatively the density of point defects and the crystalline sizes, and are useful to understand and optimize the processes of synthesis, purification, and functionalization.⁸⁵

4.2 Identifying the edges in 2D materials

Atoms at edges of 2D materials are aligned differently depending on the lattice orientation. The properties of graphene can be influenced by its edge orientation, especially in the graphene ribbon.⁹⁷ The mechanically cleaved graphene usually has two basic edge chiralities, that are, the armchair and zigzag edges.⁹⁸ Edges can be regarded as a class of defects, so the D and D' peaks could be Raman active at the graphene edge. However, owing to the translational invariance along the edge, a perfect zigzag edge cannot scatter electrons between the K and K' valleys, and the D peaks cannot appear.^{99,100} The D' peaks can be observed at both armchair and zigzag edges, because the scattering process does not involve the inter-valley scattering. At armchair edges, a strong D peak can be observed, and at zigzag edges, the D mode is forbidden.¹⁰⁰ By knowing the edge arrangement, the orientation of the whole graphene sheet can be actually determined.⁹⁸ The D intensity strongly depends on the angle between incident polarization and the armchair edge, and it is maximum for polarization parallel to the edge and minimum when perpendicular.¹⁰⁰ The intensity is proportional to $\cos^2 \theta$, where θ is the angle between the polarization direction and armchair edges. In real samples, the value of $I_{\text{D}}/I_{\text{G}}$ at the armchair and zigzag edges does not go to zero for perpendicular polarization

in both directions. This indicates that both edges in real samples are not smooth and perfect.

For anisotropic 2D materials, some forbidden Raman modes can appear at the edges and show polarization dependence, so that the edges can be characterized using polarized Raman spectroscopy.¹⁰¹ For example, B_{1g} and B_{3g} modes of BP are absent under backscattering geometry because of the lacking Raman tensor components in *x* and *z* directions. The A_g modes appear in the XX or ZZ polarization configuration, while the B_{2g} mode appears in the XZ or ZX configuration. As shown in Fig. 7(c), in the center of the BP flake, all the Raman-active phonons strictly obey the Raman selection rules. However, at the edge of the BP sample, the Raman selection rule is broken. The A_g¹ and A_g² modes appear at the edges in the XZ configuration, while the B_{2g} modes appear in the XX or XZ configuration, and the intensities depend on the types of the edge (zigzag or armchair). On the other hand, the B_{1g} and B_{3g} modes can also be observed at the edge. These can be explained by the reconstruction of edge atoms and the so-called edge phonons. For the armchair termination, the edge atoms reconstruct with atoms in the same layer moving closer together. For zigzag edges, atoms are reconstructed due to the stretching and contraction of the puckered structure along the armchair direction according to the DFT calculations.

4.3 Identifying the doping of 2D materials

Doping is an effective way to modulate the energy band structure of 2D materials. Doping can be achieved by either electrochemical or chemical approaches. Electrochemical doping can be controlled by a top-gated transistor, doping electrons or holes through voltage regulation. Chemical doping changes the carrier density by introduction of impurities and can be applied either during or after the growth process.^{102,103} After doping by electrons, holes or impurity atoms, the fermi level is modulated, and the photon–electron and electron–phonon interactions are altered, resulting in different Raman scattering processes.

For graphene, the electrochemical doping by electrons or holes can be controlled by a top-gated graphene transistor^{37,104}

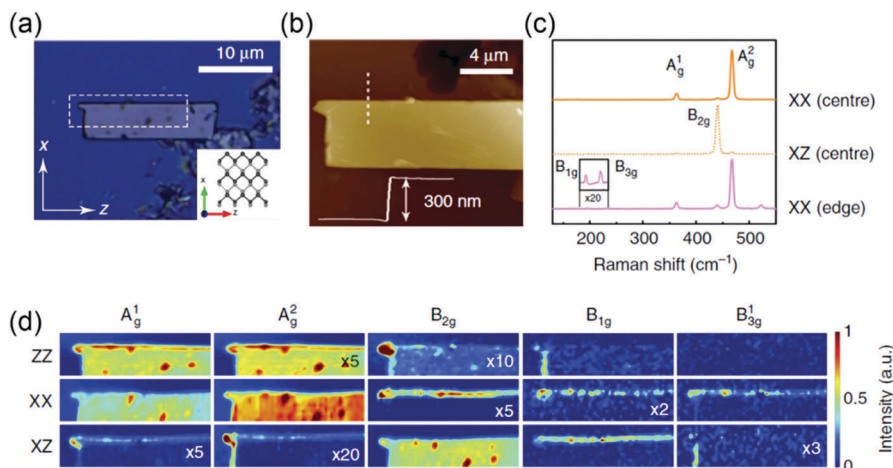


Fig. 7 (a) Optical microscope image of the measured BP flake on Si/SiO₂ substrates; the white dashed rectangle defines the area for Raman mapping measurements. The corresponding crystal orientation and crystallographic x and z axes are presented in the inset. (b) Corresponding AFM image of the measured flake. (c) Polarized Raman spectra at the center of the flake in XX (top) and XZ (middle) configurations and at an armchair edge (bottom) in the XX configuration, where the first (second) index represents the polarization of the incident (scattered) light. (d) Hyperspectral Raman intensity images of different modes under ZZ, XX and XZ configurations. Adapted with permission from ref. 101. Copyright 2016, Nature Publishing Group.

The position and line width of the first order E_{2g} band can be used to identify the presence of doping.^{49,104} The G peaks stiffen and sharpen for doping of both electrons and holes. However, the G' peak shows a different response to holes and electrons, the position of the G' peak tends to decrease for electron doping but increase for hole doping, which allows the discrimination between doping of electrons and holes. Besides, the intensity ratio between G and G' peaks $I_{G'}/I_G$ was shown to be a function of doping. Therefore, $I_{G'}/I_G$ is an important parameter to estimate the doping density of graphene.³⁷ It is worth noting that Raman spectroscopy has also been used to explore the difference in the electrochemical doping and charge transfer of graphene with molecules of the electron donor and acceptor.¹⁰⁵ As for chemical doping, such as nitrogen doping on graphene films during the growth process, there exist strong D and D' resonances in Raman spectroscopy and the intensities of the G and G' bands also change, indicating that chemical dopants act as defects in the crystal lattice.¹⁰² Further research using Raman spectroscopy reveals that nitrogen doping can actually introduce different types of defects, confirming that the surface state of graphene can be modified by nitrogen doping.¹⁰⁶

In the case of MoS₂, Raman modes also show different responses to different types of doping. In a mono-layer MoS₂ electrochemically top-gated FET, the A_{1g} mode softens and broadens with electron doping, whereas the other Raman-active E_{2g}¹ mode remains essentially inert.¹⁰⁷ In the case of thermally exposing MoS₂ to O₂, which is thought to be p-type doping, the Raman A_{1g} mode upshifts and the line width decreases.¹⁰⁸

5. Identifying the stacking of 2D materials

The stacking by van der Waals forces provides an extra freedom of degree to modulate the structure and properties of the 2D

materials.^{12,109–113} By altering the stacking order, many different material structures could be obtained, including the Bernal, rhombohedral and twisted graphene and MoX₂, the polytypism ReS₂ and heterostructures.^{9,62,114–116} The interlayer shear modes and breathing modes strongly depend on the intralayer lattice and interlayer coupling.^{61,62,115–118}

5.1 The stacking order of graphene

For multi-layer graphene, the electronic and optical properties are strongly influenced by its stacking order.^{116,119–121} Two-layer graphene usually possesses an AB Bernal structure, however, for graphene above 3 layers, ABA and ABC stacking order can both stably exist.¹²² By Raman spectra imaging on Si/SiO₂ substrates, Heinz *et al.* have proved that in 3-4L mechanical exfoliated graphene with high crystallinity, the domains with 15% of the total area display an ABC stacking order (rhombohedral stacking), while 85% of the total area are ABA stacked (Bernal stacking).¹²² The stacking order of graphene could be identified by the line shape and width of the 2D (G') peak. Taking 3L graphene as an example, the 2D peaks could be fitted by six sub-peaks, and for ABA stacked graphene, the line shape of the 2D mode shows a more symmetric feature than ABC stacked graphene as shown in Fig. 8(a), and ABC-stacked graphene exhibits a narrower width while the ABA-stacked domain presents a broader width.^{123–125} Meanwhile, the G mode of ABC stacked graphene is located at 1581 cm⁻¹, which redshifts to 1582 cm⁻¹ for ABA-stacked graphene. In contrast to the 2D mode, the width of the G modes is narrower with ABA-stacked domains than ABC-stacking domains, owing to the small difference between the phonon band structures of the two stacking order graphene.¹²⁵

Lui *et al.*¹²⁶ and Zhang *et al.*¹¹⁸ have proved that the interlayer vibration can also reveal the stacking order of graphene. The ABA stacked graphene exhibits a sharp shear mode at 33 cm⁻¹, while ABC stacked graphene does not have any peaks at 33 cm⁻¹, instead a sharp peak at 19 cm⁻¹ was observed.

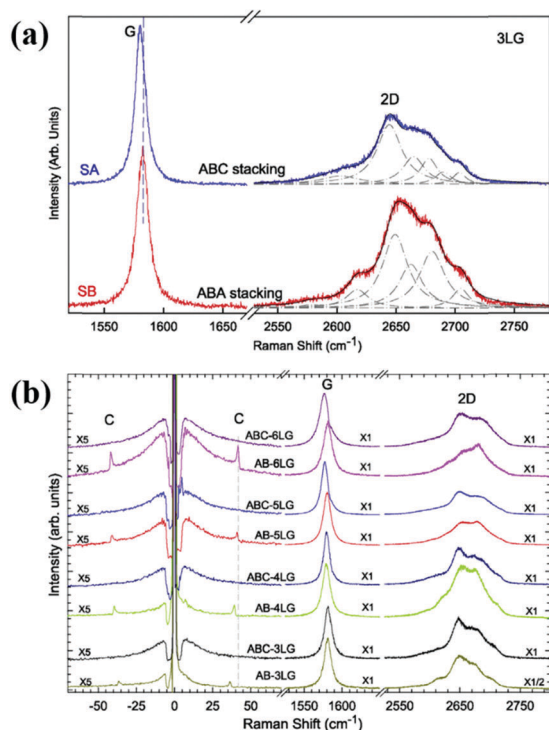


Fig. 8 (a) Raman spectra of 3LG measured at two different spots on Si/SiO₂ substrates. Dash-dotted lines are the fits to the 2D mode in ABA- and ABC-3LG. (b) Raman spectra of AB- and ABC-NLG ($N = 3, 4, 5, 6$) in the C, G and 2D peak spectral regions. The shear modes are observed in AB-NLG ($N = 3, 4, 5, 6$), but not in ABC-NLG. Adapted with permission from ref. 118. Copyright 2016, Elsevier.

For 3–6 layer graphene, the highest-frequency shear mode in AB-stacked graphene can also be observed, but not in

ABC-stacked graphene, as shown in Fig. 8(b).¹¹⁸ In ABA stacked graphene, the vanishing of the low frequency shear mode is owing to the polarization configuration, and in ABC stacking, the high frequency shear mode belongs to E_{2u} , which is Raman inactive.

For AB-stacked bilayer graphene, the energy band structure displays quadratic dispersion with two parallel parabolic conduction and valence bands.^{127–129} But for twisted bilayer graphene, when the twisted angle is greater than 1.5° , the energy band structure is split.^{127,130,131} Phonons also behave differently from that in single layer graphene. Chen *et al.* have investigated the thermal conductivity of suspended twisted bilayer graphene, and found that it was lower than that of monolayer graphene in the temperature range of 300–700 K.⁵

Fig. 9(b) shows the Raman spectrum of twisted bilayer graphene with different twisted angles at 532 nm excitation wavelength on Si/SiO₂ substrates.¹³² Most of the twisted bilayer graphene show similar Raman features to single layer graphene. However, when the twisted angle is about 12° , the intensity of the G peak is greatly enhanced by tens of times owing to the resonance effect. The peak widths of G and 2D bands are much broader than that of single layer graphene at small twist angles, decrease with increasing angle but increase at the resonant angle.¹³³ The widths then further decrease to that of single layer graphene at an angle of 30° .^{132,134} The first Brillouin zone of twisted bilayer graphene is shown in Fig. 9(a) and (b) shows the overlap of the Dirac ones which leads to the appearance of van Hove singularity.¹³⁴ The energy gap between van Hove singularities changes with the twisted angle.¹³⁵ For a laser of fixed wavelength, the critical twisted angle can be calculated as follows:¹³⁴

$$\theta_c = \frac{3aE_{\text{laser}}}{\hbar v_f 4\pi}$$

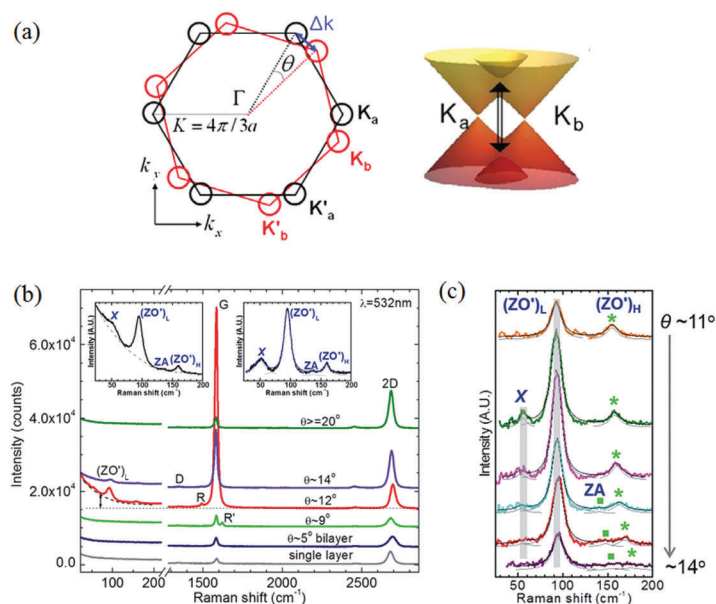


Fig. 9 (a) Left: Schematic diagram of the first Brillouin zone for twisted bilayer graphene at twist angle θ . Right: Raman scattering process that contributes to the intensity of the G peak. Adapted with permission from ref. 134. Copyright 2012, APS Physics. (b) Raman spectra of bilayer graphene at different twist angles excited by 532 nm laser on Si/SiO₂ substrate. (c) Background-subtracted low-frequency Raman spectra at different twist angles ranging from 11° to 14° .¹³² Adapted with permission from ref. 132. Copyright 2013, ACS Publications.

where a is the lattice constant of graphene, \hbar is the Planck constant, and v_f is the Fermi speed of single layer graphene. For an excitation wavelength of 532 nm (2.33 eV), the critical twisted angle is $\theta_c = 12^\circ$, which agrees well with the experimental results. If the twisted angle is further increased, the resonant excitation occurs only in a single Dirac cone, and the Raman spectrum is expected to be similar to that of single layer graphene.

In addition to the peak widths of G and 2D peaks, two new Raman modes, that are R and R' modes which correspond to the TO and LO phonons, also appear with angle dependent peak positions.^{26,136,137} These two modes originate from the superlattice produced by rotation and are double resonant scattering processes. Furthermore, in the low frequency range, an out-of-plane acoustic mode (ZA) and an interlayer breathing mode (ZO') can be observed as well. Fig. 9(c) shows the background-subtracted Raman spectra at different twisted angles ranging from 11° to 14° . In the range of $130\text{--}180\text{ cm}^{-1}$, two peaks appear at about 150 and 180 cm^{-1} (ZA and (ZO')_H) and blueshift with an increasing twist angle.¹³² In the vicinity of 94 cm^{-1} , there is also a peak labelled as (ZO')_L. When the twist angle is near θ_c , both the frequency and FWHM greatly change and the intensity of (ZO')_L reaches the maximum due to resonance enhancement. These modes have been well-studied by a few groups.^{29,138} For example, Tan's group investigated the interlayer interaction of twisted multilayer graphene by multi-wavelength Raman scattering measurements.¹³⁹

5.2 The stacking order of TMDs

In layered transition metal dichalcogenides (TMDs), different stacking orders lead to several polytypism with different crystal-line symmetry.¹⁴⁰ The two typical polytypisms of MX_2 ($X = \text{S}, \text{Se}$) are 2H- MX_2 (D_{3h}) and 3R- MX_2 (C_{3v}).^{41,141,142} Cheong *et al.*¹⁴⁰ investigated the Raman spectra of 2H- and 3R- MoS_2 on Si/SiO₂ substrates, and the low-frequency interlayer modes of MoS_2 indicate different stacking orders. The lowest interlayer breathing mode of 3 layers 2H- MoS_2 locates at $\sim 28\text{ cm}^{-1}$, while the lowest breathing modes of 3R- MoS_2 redshift to 25 cm^{-1} with a 2.41 eV (514.5 nm) excitation energy owing to the weaker

interlayer interaction, and the shear modes do not show an obvious stacking order dependence.

For MoSe_2 , the low frequency Raman features are also correlated to the stacking orders as shown in Fig. 10.¹⁴³ In the cross polarization configuration, the interlayer breathing modes of both 2H- and 3R MoSe_2 are forbidden, while the shear modes are still active and are called S_1, S_2, S_3, \dots from the highest frequency mode to the lowest frequency mode. In 2H- MoSe_2 , only the odd interlayer modes (S_1, S_3, S_5, \dots) can be observed. Moreover, the peak intensities of all the observable shear modes in 2H follow the trend $I(S_1) > I(S_3) > I(S_5), \dots$. However, in 3R- MoSe_2 , the peak intensities have an opposite tendency, that is, the shear modes with lowest frequency exhibit the highest intensity, and $I(S_5) > I(S_3) > I(S_1), \dots$. These features can be used for identifying the stacking order of MoSe_2 , and this method may also be applicable to other TMD materials with a similar crystal structure and optical properties.

Twisted bilayer transitional metal dichalcogenides (TMDs) have been extensively studied using photoluminescence spectroscopy.^{63,144,145,146} For example, the PL intensity ratio between the trion and the exciton was found to be the maximum for twist angles of 0° and 60° , but minimum for angles of 30° or 90° .¹⁴⁵ On the other hand, the Raman modes of TMDs are also affected by the interlayer electronic coupling, especially for the low frequency modes that are more sensitive to the interlayer coupling.⁶³ Fig. 11 shows the Raman spectra of MoS_2 in both the high and low frequency ranges.¹¹⁷ The high frequency modes A_{1g} and E_{2g} exhibit a weak dependence on the twist angle when compared with that of monolayer MoS_2 or exfoliated bilayer MoS_2 . However, the Raman modes at 23 cm^{-1} and 38 cm^{-1} corresponding to the interlayer shear mode (S) and breathing mode (B), respectively, show a strong dependence on the twist angle. As can be seen from Fig. 11(a), the intensity of the shear mode is lower than the breathing mode, and both of them disappear for monolayer MoS_2 , further confirming that these modes come from the vibration between two layers. For exfoliated bilayer MoS_2 , it shows a stronger shear mode, a weaker breathing mode and a higher frequency than artificially constructed twisted bilayer MoS_2 . Besides, the shear mode and breathing mode show

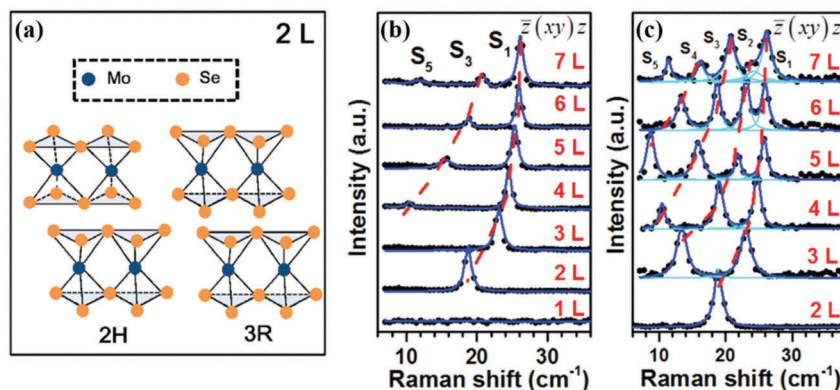


Fig. 10 (a) Schematic of 2H and 3R- MoSe_2 stacking in 2 L. (b) Low frequency Raman spectra of 2H- MoSe_2 . (c) Low-frequency Raman spectra of 3R- MoSe_2 . The samples are deposited on Si/SiO₂ substrates. Black lines/dots are experimental data and blue lines are fitting results using Lorentzian function. Adapted with permission from ref. 143. Copyright 2015, Wiley.

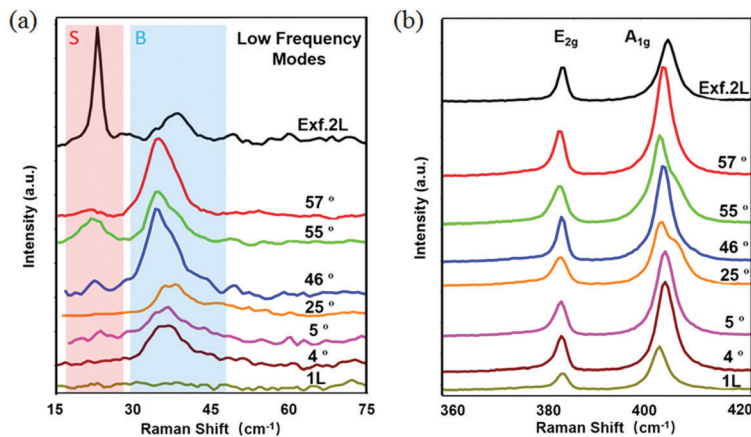


Fig. 11 (a) Low frequency and (b) high frequency Raman spectrum of twisted bilayer MoS₂ on Si/SiO₂ substrates at different twisted angles in the range of 60° period. Adapted with permission from ref. 117. Copyright 2016, ACS Publications.

different dependence on the twist angle, which has also been found in other TMD materials.¹¹⁷

5.3 Interlayer coupling in anisotropic 2D materials

Different from isotropic 2D materials like graphene and MoS₂, the shear modes of anisotropic materials are non-degenerate due to the low symmetry of the crystal structure, and the interlayer modes also exhibit polarization dependence.^{61,62,118,147,148}

In *N*-layered (NL) BP, there are *N* – 1 interlayer shear modes vibrating along the zigzag direction, *N* – 1 interlayer shear modes along the armchair direction (B_{1g}, B_{2g} or B_{1u}, B_{3u}) and *N* – 1 interlayer breathing modes along the out-of-plane direction (A_g or B_{2u}). Furthermore, the number of breathing modes (B modes) with Raman-active A_g symmetry is *N*/2 for even *N* and (*N* – 1)/2 for odd *N*.⁶¹ Under backscattering geometry, the shear modes of BP are forbidden according to the Raman selection rules. It can be seen that the frequencies of the Raman

peaks depend on the sample thickness, so the low frequency Raman modes of BP can be used to identify the layer number of the sample.¹⁴⁸ There are two types of breathing modes as shown in Fig. 10(a).⁶⁰ For B^H modes, with increasing thickness, the frequencies of Raman peaks blueshift clearly, and can be fitted by the standard linear chain model: $\omega = \omega_0 \sqrt{1 \pm \cos(\pi/N)}$. For CBM modes, with increasing thickness, the Raman peaks redshift which is not coincident with the linear chain model, but can be fitted by $\sqrt{1/N}$. The results indicate that the B^H modes are generated by the vibration between BP layers, but the CBM modes originate from the vibration of the whole BP layers and the substrate, so the strong interlayer coupling of BP can be proven. Furthermore, the low-frequency breathing modes (A_g) of BP also exhibit a strong polarization dependence and the maximum is reached when the polarization direction is parallel to the principal axis.⁶¹

Multilayer ReS₂ has different stacking orders and can be proven by the ultra-low frequency Raman spectra. Two stable

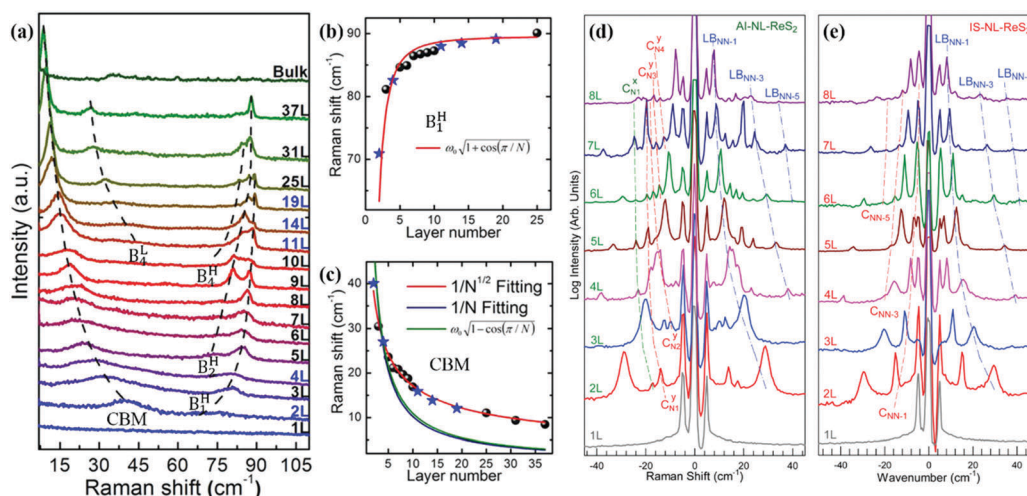


Fig. 12 (a) Raman spectra of BP samples with different thicknesses on Si/SiO₂ substrates. CBM denotes the collective breathing mode, and B_{*n*}^H (B_{*n*}^L) denotes the *n*th-order breathing mode from the higher (lower) branch. Layer number dependence of (b) CBM and (f) B_{*n*}^H modes. Adapted with permission from ref. 60. Copyright 2016, APS Physics. (d and e) Stokes/anti-Stokes Raman spectra in the C and LB peak region for Al-stacked (d) and IS-stacked (e) 2–8L ReS₂ along with that of 1L ReS₂ on Si/SiO₂ substrates. Adapted with permission from ref. 115. Copyright 2016, RSC Publishing.

stacking orders have been demonstrated and named as isotropic-like (IS) and anisotropic-like (AI) N layer (NL, $N > 1$) ReS_2 .¹¹⁵ As shown in Fig. 12(d), in AL-NL- ReS_2 , two shear modes (C modes) can be observed. In AL-2L- ReS_2 , the frequencies of C_{21}^y , C_{21}^x and LB_{21} are 12.8 cm^{-1} , 16.9 cm^{-1} , 26.5 cm^{-1} , and the frequency difference of 4.1 cm^{-1} between the C_{21}^y and C_{21}^x is very obvious to distinguish the two Raman peaks. While for the IS-2L- ReS_2 flakes, only one shear mode can be observed at 15.1 cm^{-1} , because of the negligible difference between the frequency of the shear modes. For both AL-NL- ReS_2 and IS-NL- ReS_2 , the changing of the Raman shifts with increasing thickness could be explained by the linear chain model and the force constant of the shear modes and breathing modes could also be calculated from the ultra-low frequency Raman spectra.^{62,118}

5.4 Interlayer coupling in 2D van der Waals heterostructures

Different from the twisted bilayer 2D materials, the van der Waals heterostructure by stacking different materials together exhibit new characteristics that are not possible for one single material.

The wide band gap h-BN nanosheets are suitable to form heterostructures with other 2D layered materials for optoelectronics or as a dielectric substrate for high-performance electronics.^{149,150} For graphene/h-BN heterostructures, a characteristic broadening of the 2D peak of graphene/h-BN superlattices has been observed and can be used to identify graphene superlattices with a misalignment angle smaller than 2° .¹⁵¹ In MoS_2 /h-BN vertical van der Waals heterostructures, the blue shift of E_g^1 and A_{1g} modes of MoS_2 on the h-BN film show the smaller lattice strain and lower doping levels than those directly grown on SiO_2 , which can boost the performance of intrinsic TMDs.¹⁵²

Recently, Tan's group investigated the low-frequency Raman spectroscopy of the MoS_2 /graphene heterostructure on Si/ SiO_2 substrates.²⁹ Fig. 13(a) shows the shear and breathing modes of

multilayer MoS_2 /1L graphene, along with the E_{2g} and A_{1g} modes, and the grey curve is the Raman spectrum of intrinsic multilayer MoS_2 . The peak position of E_{2g} and A_{1g} of the heterostructure exhibits a blue shift and a red shift respectively. In the low frequency range, the shear modes and breathing modes of monolayer MoS_2 /monolayer graphene cannot be observed owing to the weak coupling of electrons and phonons. Fig. 13(b) shows the Raman spectra of the breathing mode of the multilayer MoS_2 /1L graphene heterostructure and intrinsic multilayer MoS_2 in parallel(XX)-cross(XY) polarization configurations.²⁹ There is an obvious redshift for the breathing mode of the heterostructure compared to that of intrinsic MoS_2 . Fig. 13(c) summarizes the frequency difference of A_{1g} and E_{2g} breathing modes and shear modes between the heterostructure and corresponding MoS_2 as the number of layer changes.²⁹ It can be seen clearly that the breathing mode is more sensitive to the interlayer coupling than the other three modes. This is also confirmed by other groups,¹⁵³ and it has been further proven that the interlayer coupling of van der Waals is not sensitive to the twist angle.¹⁵⁴

6. Identifying the differences on the nanoscale

Scanning probe microscopy (SPM) characterizes the morphology of materials with nanoscale spatial resolution. If combined with Raman spectroscopy, Raman scattering information can be obtained with same spatial resolution. This is achieved by tip-enhanced Raman spectroscopy (TERS) using a metallic tip, that is, the same tip for scanning tunnelling microscopy (STM) or the metal coated atomic force microscopy (AFM) tip. A strong local electromagnetic field is confined tightly at the tip due to the excitation of localized surface plasmons by the incident laser, which further excite the Raman scattering in the near field. TERS has been widely applied in different fields including

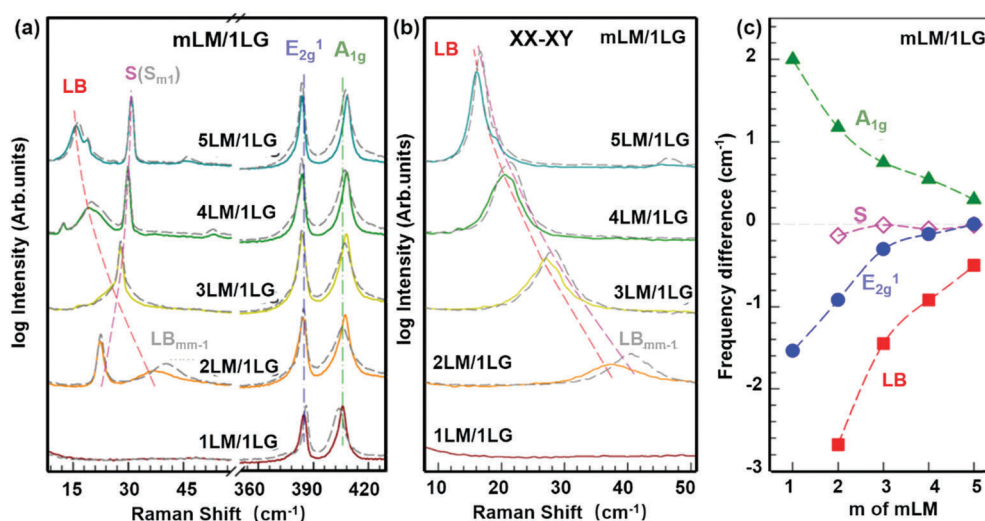


Fig. 13 (a) Low frequency and high frequency Raman spectra of different layers MoS_2 and the monolayer graphene heterostructure on Si/ SiO_2 substrates. (b) Raman spectra of the LB modes in the multilayer MoS_2 /monolayer graphene heterostructure along with those of pristine multilayers MoS_2 used as reference in gray dashed curves. (c) The peak position differences of shear, breathing, A_{1g} , and E_{2g} modes between the heterostructure and corresponding intrinsic multilayers MoS_2 . Adapted with permission from ref. 29. Copyright 2017, ACS Publications.

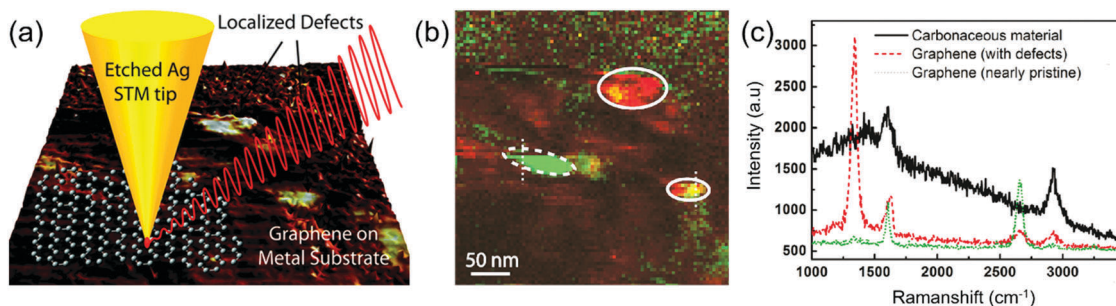


Fig. 14 (a) Schematic illustration of TERS measurement of graphene. (b) The Raman mapping image of graphene on template-stripped gold. The red region indicates the mapping of D band and the green region indicates the 2D band of graphene. (c) The corresponding Raman spectra of the red, green and black areas in (b). Adapted with permission from ref. 155. Copyright 2011, ACS Publications.

materials science, biology, physics for characterization of samples with nanoscale or even atomic resolution, and a number of publications have reported the TERS characterization of 2D materials.^{38,155–163}

Stadler *et al.*¹⁵⁵ reported the chemical imaging of monolayer graphene on the nanoscale using TERS. Fig. 14(a) shows the schematic illustration of the TERS measurement on graphene. In Fig. 14(b), the overlaid TERS images of the 2D (red) and D (green) bands of single layer graphene mechanically exfoliated on template-stripped gold surface are shown in an area of $400 \times 400 \text{ nm}^2$. Fig. 14(c) shows the corresponding TERS spectra of the red, green and black areas in Fig. 14(b). The dimensions of the two defects are $75 \times 45 \text{ nm}^2$ and $55 \times 25 \text{ nm}^2$, respectively, and the spatial resolution, determined from the FWHM of the curve fitting of the line profiles indicated by the white dotted lines in Fig. 14(b), was found to be 10.6 nm and 11.8 nm for the 2D and D bands, respectively. Mignuzzi *et al.*¹⁵⁶ studied the distribution of point defects created in graphene by means of Bi_3^+ ion bombardment. The average distance between point defects, L_D , was measured to be about 130 nm using TERS. Compared to the measured value of $L_D = 100 \pm 40 \text{ nm}$ using far field Raman characterization described above, this value is more accurate and was obtained directly from Raman mapping images. On the other hand, the enhancement factors of D, G and 2D bands in TERS were compared, and the D band showed the largest enhancement (~ 1.5 times stronger than G band) due to its out-of-plane vibrations that are parallel to the local electric fields at the tip and are preferentially enhanced.

Beams *et al.*¹⁵⁸ obtained the TERS mapping image of the 2D peak of graphene with a single 5 nm particle on the surface. Since the 2D peak is sensitive to strain in graphene, the information on local strain was extracted with a spatial resolution of 34 nm. Fig. 15(a) shows the AFM image of the corresponding area, and the height profile of the particle along the dashed arrow is shown in Fig. 15(b). In Fig. 15(c), the peak shift of the 2D band was plotted along the dashed line indicated in Fig. 15(a). It is seen that under local strain induced by the nanoparticle, the 2D peak redshifts and is broadened by 4 cm^{-1} . The strain is also confirmed to be in radial directions. The quantitative analysis of the strain distribution is performed. The strain in the radial direction (r) is linearly dependent on $r^{-2/3}$ through Schwerin's equation. The

derived strain is plotted in Fig. 15(c) (right y-axis). Local strain in other 2D materials has also been studied using TERS, for example, Park *et al.*¹⁵⁹ used both TERS and tip-enhanced photoluminescence spectroscopy to characterize the strain in WSe_2 .

Taking advantage of the high spatial resolution, edges, wrinkles and grain boundaries in 2D materials can be better investigated using TERS. Ghislandi *et al.*¹⁶⁰ studied the edges of mechanically exfoliated graphene using TERS. They found that the Raman enhancement of the D band at the edges was ~ 5.6 times compared to that measured using confocal Raman spectroscopy. The enhancement is dependent on the polarization of incident laser and the vibrational directions of the Raman modes. Park *et al.*³⁸ also measured the grain boundaries in graphene using TERS with a spatial resolution of 18 nm. Fig. 15(d) shows the AFM image of graphene, and the corresponding TERS image of the 2D peak is shown in Fig. 15(e), where the grain boundaries can be clearly seen. From the change of the intensity, peak width and the center position of the 2D band, Coh *et al.*¹⁶¹ were able to quantitatively determine the misorientation angles of three bilayer grain boundaries A (5°), B (8°), and C (14°), as shown in Fig. 15(f).

Rahaman *et al.* used TERS to investigate the strain caused by gold nanostructures on few layer MoS_2 .¹⁶⁴ As shown in Fig. 16(a), a periodic array of gold nanotriangles (Au NTs) with a 120 nm side length and a 40 nm height was arranged on a silicon substrate. Then few layer MoS_2 was transferred onto the array. Fig. 16(b) shows the TERS intensity mapping on the area of interest with a spatial resolution of $< 25 \text{ nm}$. The averaged tip-enhanced Raman spectra of each circle marked in Fig. 16(b) were exhibited in Fig. 16(c), where the E_{2g} and A_{1g} modes of MoS_2 were labelled. Through fitting the Raman peaks by Voigt functions in Fig. 16(c), the peak positions of $E_{2g}(\Gamma)$ and $A_{1g}(\Gamma)$ modes of each curve are obtained and shown in Fig. 16(d). Thus, the averaged frequency shift measured at the corners of the triangles with respect to the valley among the triangles of $E_{2g}(\Gamma)$ and $A_{1g}(\Gamma)$ modes are shown in Fig. 16(d). The shift of the $E_{2g}(\Gamma)$ mode was about $(2.6 \pm 0.7) \text{ cm}^{-1}$ which indicates 0.9% strain in the nanoscale region. The shift of the $A_{1g}(\Gamma)$ mode is about 0.2 cm^{-1} which is smaller than the error limit of the fitting, thus can be ignored. It is explained that strain and doping effects partially cancel out in inducing the frequency shift of the $A_{1g}(\Gamma)$ mode.

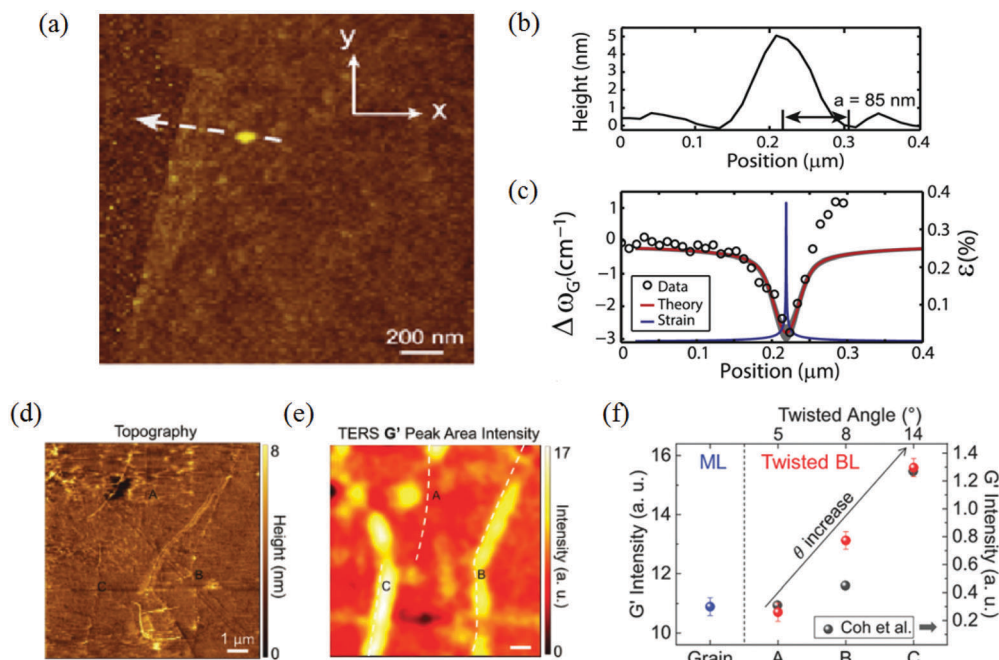


Fig. 15 (a) AFM image of graphene with a nanoparticle on the surface. (b) Corresponding height profile of the nanoparticle along the dashed line in (a); (c) plot of the Raman shift of the 2D-peak (circles) profile along the white arrow in (a). The fit is shown in red and the total strain profile is shown in blue. Adapted with permission from ref. 158. (d) The AFM image of grain boundaries on graphene, marked as A, B and C. (e) Corresponding G' (2D) peak intensity distribution in the zone of c obtained by TERS mapping. (f) Measured intensity of G' peak at grain boundaries (red circles) from (d) is compared with the calculated values¹⁶¹ (gray circles). Adapted with permission from ref. 38. Copyright 2017, Wiley.

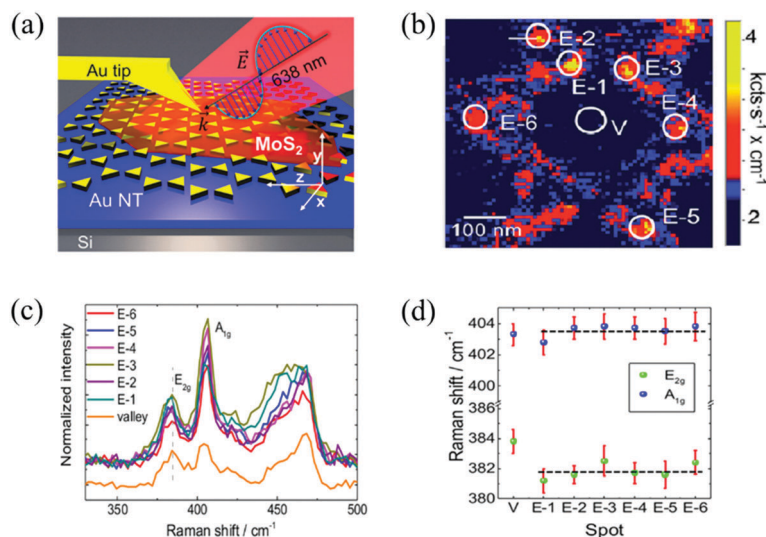


Fig. 16 (a) Schematic of the TERS experiment. The few layer MoS₂ was transferred onto the gold nanotriangle array. (b) The TERS intensity mapping of one hexagonal structure. The Raman signal of MoS₂ is enhanced in the vicinity of gold corners. (c) The averaged Raman spectra obtained from each labeled circle in (b). (d) Raman peak positions of E_{2g}(I) and A_{1g}(I) modes are extracted from each curve in (c). The black lines represent the average values of the peak positions. Adapted with permission from ref. 164. Copyright 2017, ACS Publications.

7. Probing the charge interaction between 2D materials and molecules via Raman enhancement

van der Waals heterostructures of 2D materials provide a platform to study the charge interactions at the interface and

render new possibilities for novel optoelectronic device applications.^{27,165–167} As a matter of fact, the charge interaction between organic molecules and 2D materials has also drawn enormous attention.¹⁶⁷ Such interactions can be revealed using Raman spectroscopy either from the frequency shift or the intensity enhancement.^{168–170} For example, if electron-donor molecules are on the surface of graphene, the G band of

graphene will redshift, whereas if it is electron-acceptor molecules, the G bands will blueshift, as discussed earlier as the doping effect.^{171–178}

The Raman intensity of molecules on the surface of most 2D materials can be enhanced due to the charge interactions between molecules and the material, which lead to the modulation of effective polarizability of the molecules. The 2D materials that have been studied for Raman enhancement include graphene, h-BN, MoS₂, orthorhombic BP and triclinic ReS₂.¹¹⁸

7.1 Charge transfer between graphene and molecules

The direct spectroscopic evidence of the charge interaction between molecules and graphene is the photoluminescence quenching of fluorescent dyes (rhodamine 6G, R6G; and protoporphyrin IX, PPP) adsorbed on graphene.¹⁷⁹ Furthermore, it was reported that graphene can enhance the Raman signals of adsorbed molecules, as illustrated in Fig. 17(a) and (b), which is known as graphene-enhanced Raman scattering (GERS).^{180,181} As the surface plasmon resonance frequency of graphene is in the terahertz region, there is no electromagnetic enhancement for the molecules. Hence, the chemical effect, that is, the charge transfer, is responsible for the Raman enhancement of molecules. It has been reported that effective charge transfer occurs between molecules with a large electron conjugation, such as R6G, PPP and Pc, which interact with graphene through strong π - π interactions and charge interactions from the N atoms with lone pair electrons. Many studies have confirmed the charge interaction between molecules and graphene that gives rise to the Raman enhancement of GERS. For example,

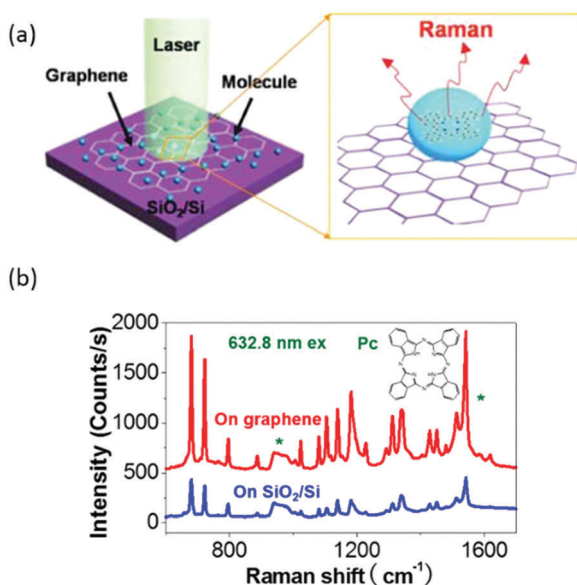


Fig. 17 (a) Schematic illustration of the molecules on graphene and a SiO₂/Si substrate, and the Raman experiments. (b) Comparisons of Raman signals of Pc deposited 2 Å on graphene (red line) and on the SiO₂/Si substrate (blue line) using vacuum evaporation at 632.8 nm excitation except for the peak marked by the star (*) (the 960 cm⁻¹ peak from Si, and the 1586 cm⁻¹ peak from graphene), all the peaks are from Pc. The inset in (b) shows the structure of Pc. Adapted with permission from ref. 180. Copyright 2010, ACS Publications.

the first-layer effect that means only the first layer of molecules on graphene is mostly enhanced;¹⁸² the modulation of the Fermi level of graphene by external electric field tunes the Raman enhancement of molecules.^{183,184}

The orientation of molecules on graphene, that is, molecules in the lying-down or the standing-up configuration, strongly affects the efficiency of charge transfer, and this can be seen from the Raman enhancement of molecules.¹⁸⁵ For example, copper phthalocyanine (CuPc) molecules can be deposited on graphene using the Langmuir–Blodgett technique, which results in the upstanding configuration. After annealing, the CuPc molecules change orientation to lying-down as shown in Fig. 18(a), and the Raman spectra of CuPc in the two different orientations are shown in Fig. 18(b) and (c). It is seen that the Raman intensity of the CuPc molecules on graphene was largely enhanced after annealing, due to the overlay of π -orbitals of molecules and graphene and the change of the interface dipole. As illustrated in Fig. 18(d) and (e), interfacial dipoles are induced at the CuPc/graphene interface, which leads to a shift of the energy level of the CuPc molecules at the interface and the increase of the possibility of optical transition. What is more, the Raman enhancement factor varies from different vibration modes, for example, the mode at 1530 cm⁻¹ is more enhanced than that at 1450 cm⁻¹, because the vibration of the 1530 cm⁻¹ mode is related to larger displacement of the N atoms with lone pair electrons. Huang *et al.* systematically compared a series of molecules: those with similar molecular structures but different energy levels which refers to different Pc derivatives and those with similar energy levels but different molecular structures, such as tetrathienophenazine (TTP) and tris(4-carbazoyl-9-ylphenyl) amine (TCTA).¹⁸⁶ They show that molecular symmetry and substituents similar to that of the graphene structure exhibit larger Raman enhancement, which is due to the effective π - π interaction between molecules and graphene. By analyzing the enhancement factors of all these molecules on graphene and their energy differences between HOMO (or LUMO) and graphene's Fermi level, it can be concluded that the enhancement involving molecular energy levels requires the HOMO and LUMO energies to be within a suitable range with respect to graphene's Fermi level.¹⁸⁷ Joo *et al.* also designed a series of dipolar molecules with the same general structure of *N*-ethyl-*N*-(2-ethyl(1-pyrenebutyrate)-4-(4-*R*-phenylazo)aniline) where the *R* groups varied from electron-withdrawing group or electron-donating group, and thus alter the magnitude of the dipole moment and hence the electronic coupling of chromophores with graphene.¹⁸⁸ DFT calculations reveal that the energy gap decreases rapidly with increasing dipole moment, which is also in agreement with the observed trends in the frequency shift of G band.

7.2 Charge interaction between molecules and other 2D materials

Ling *et al.* compared the Raman enhancement effect of CuPc molecules on graphene, h-BN and MoS₂.¹⁸⁹ It is found that the high-frequency Raman modes of CuPc are enhanced more strongly on graphene than that on h-BN, while the low-frequency Raman

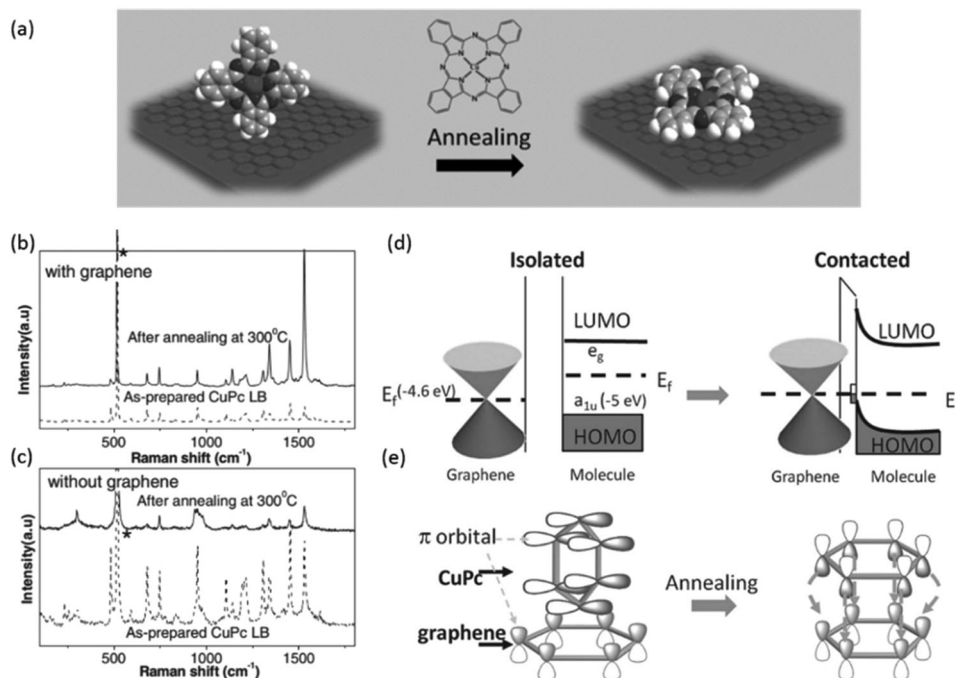


Fig. 18 (a) Schematic illustration of molecular orientation change under annealing. Inset: The molecular structure of CuPc. (b) Comparison of Raman spectra of as-prepared CuPc LB film (dashed line) and that after annealing at 300 °C (solid line) on a SiO₂/Si substrate with graphene (c) similar to (b) but without graphene. Schematic illustrations of (d) the change of the electron energy band between graphene and the molecule before and after contact, and (e) the relative direction of the delocalized π orbital of graphene and the CuPc molecule before and after annealing. Adapted with permission from ref. 185. Copyright 2012, Wiley.

modes of CuPc are weaker on graphene. MoS₂ demonstrates the weakest overall Raman enhancement among these three materials. The results are ascribed to different types of charge interactions: (1) graphene has a zero bandgap; (2) h-BN is insulating and has a strong B–N bond, while (3) MoS₂ is semiconducting with the sulfur atoms on the surface and has polar covalent bonds (Mo–S) with the polarity in the normal direction to the surface. In this regard, the different charge interactions are proposed: (1) charge transfer occurs between molecules and graphene; (2) strong dipole–dipole coupling may occur between molecules and h-BN, and (3) both charge transfer and dipole–dipole coupling may occur but with a weaker magnitude for MoS₂.

The in-plane symmetry of 2D materials strongly affects the charge interactions. The recent renaissance of anisotropic 2D layered materials, such as BP and ReS₂, has triggered a novel dimension to investigate the symmetry dependent properties and polarization-dependent optoelectronic applications.^{23,24,66,68,190,191} The carrier mobility, optical absorption, thermal conductivity are strongly dependent on the crystalline orientation of the materials. Lin *et al.* studied the Raman enhancement of CuPc molecules on BP and ReS₂ using angle-resolved polarized Raman spectroscopy (ARPRS).⁷⁰ It can be found in Fig. 19 that the Raman signals of CuPc molecules on BP are enhanced compared to that on blank SiO₂/Si substrates. More interestingly, the Raman spectra of CuPc molecules exhibits a strong polarization dependence in both parallel and cross polarization configurations, which is absent on SiO₂/Si substrates. Polar plots of the normalized intensities of 468 cm⁻¹ (BP, A_{2g}²), 682 cm⁻¹ (CuPc, A_{1g}), 1450 cm⁻¹ (CuPc, B_{2g}), 1530 cm⁻¹ (CuPc, B_{1g}) modes show periodic changes as a

function of sample rotation angle. The maximum intensity angles of the B_{1g} mode coincide with the armchair (AC) direction of BP, which agrees well with Raman tensor analysis of uniformly aligned CuPc molecules. However, the orientation of molecules is random owing to the use of the thermal evaporation method for deposition. Density function theory (DFT) calculations show that the charges at the conduction band minimum and covalence band maximum are redistributed into one-dimensional chains along the AC direction of BP with the deposition of CuPc. For graphene, the charge distributions remain isotropic with or without molecules. That is, CuPc induced the anisotropic charge redistribution of BP, resulting in anisotropic charge interactions, and only the CuPc molecules with a major axis parallel to the AC direction of BP have the highest probability of charge interactions and exhibit the largest Raman enhancement, which dominate the angle dependence of the Raman intensities.

7.3 Charge interactions between molecules and heterostructures of 2D materials

As mentioned above, different 2D materials exhibit different charge interaction mechanisms with molecules for Raman enhancement. Heterostructures may provide more tenability of the charge interactions. Tan *et al.* designed a 2D graphene/WSe₂ (G/W) heterostructure as a novel platform for Raman enhancement and found that the intensity of the Raman scattering on G/W is much stronger compared with isolated layers.¹⁹² Through DFT calculations and probe–pump measurements, it is inferred that the electronic state density of graphene is increased due to the coupling with WSe₂ and finally increases the electronic density

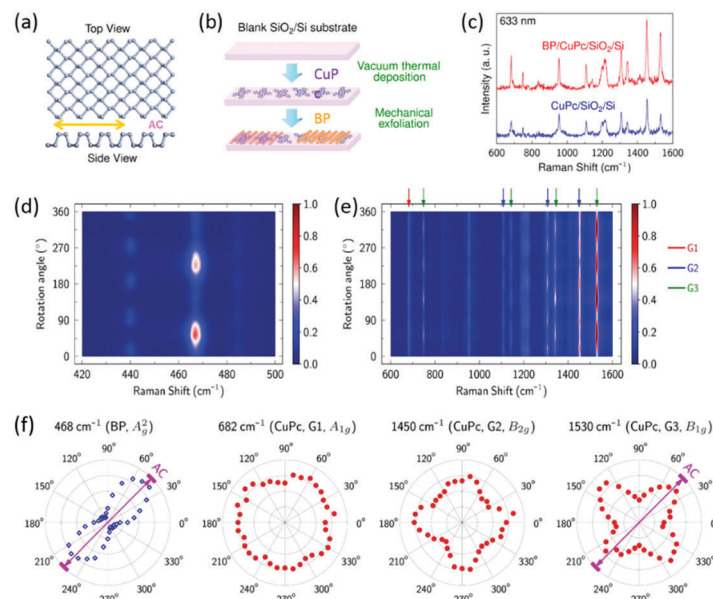


Fig. 19 (a) Top and side view of orthorhombic BP. The armchair direction of BP is denoted AC and marked by the double-arrow. (b) Schematic illustration of the sample preparation procedure. (c) Raman spectra of CuPc molecules on a 300 nm SiO₂/Si substrate with (upper curve) and without (lower curve) few-layer BP on top. (d and e) Angular dependence of the normalized Raman spectra of BP (d) and CuPc molecules with BP (e), respectively. (f) Polar plots of the normalized intensities of 468 cm⁻¹ (BP, A_g²), 682 cm⁻¹ (CuPc, A_{1g}), 1450 cm⁻¹ (CuPc, B_{2g}), 1530 cm⁻¹ (CuPc, B_{1g}) modes as a function of sample rotation angle measured on BP. The AC direction of BP is marked by the double-arrow. Adapted with permission from ref. 70. Copyright 2015, ACS Publications.

of states ($g(E_k)$) at the interface between the molecule and graphene, while only a negligible gap is caused by the interaction between graphene and WSe₂ which does not affect the energy matching between energy levels of CuPc molecules and the Fermi level of graphene, indicating little influence on the charge transfer.

8. Summary and outlook

Among all the optical spectroscopic characterization methods, Raman spectroscopy can provide both structural and electronic band information, and has been one of the most important characterization tools for 2D materials. A slight change in the lattice structure of 2D materials will lead to a significant change in the Raman features, and a variation in the electronic properties due to doping, interlayer coupling and electronic coupling with molecules will also change the Raman frequencies and intensities. In this review, the recent advances in Raman spectroscopic characterization of 2D materials were mainly discussed, including the polarized Raman scattering of anisotropic 2D materials, the effects of defects, doping and stacking. The use of TERS for high spatial resolution characterization and the Raman enhancement effect of 2D materials were also discussed. This review emphasizes more on the characterization aspect of structural and electronic differences from the primitive 2D materials using Raman spectroscopy.

With the discovery of new 2D materials, the characterization of the structures and properties is essential for the fundamental understanding of the materials. On the other hand, the possible applications of the materials, either in the primitive form or functionalized form, are even more intriguing. Great efforts have been made in the improvement of quality during synthesis, the

chemical functionalization of materials and the construction of heterostructures and working devices. Another reason that Raman spectroscopy is becoming a routine characterization tool for 2D materials is that it can be used to measure samples during all these stages *in situ* or *ex situ*. Along this line, the development of techniques for *in situ* Raman measurements adapting to various conditions for more convenient and more reliable characterization, and techniques for the measurement of low frequencies for fundamental research, can be expected to be the future directions for Raman characterization of not only 2D materials, but also new materials in general.

Conflicts of interest

There are no conflicts to declare.

Acknowledgements

This work was supported by the Ministry of Science and Technology of China (2016YFA0200100 and 2015CB932400), the National Natural Science Foundation of China (Grant No. 51432002, 51720105003, 21790052, 11374355 and 21573004), and the Beijing Municipal Science and Technology Project (Grant No. Z161100002116026).

References

- 1 K. S. Novoselov, A. K. Geim, S. V. Morozov, D. Jiang, Y. Zhang, S. V. Dubonos, I. V. Grigorieva and A. A. Firsov, *Science*, 2004, **306**, 666–669.

- 2 R. R. Nair, P. Blake, A. N. Grigorenko, K. S. Novoselov, T. J. Booth, T. Stauber, N. M. R. Peres and A. K. Geim, *Science*, 2008, **320**, 1308.
- 3 C. L. Kane, *Nature*, 2005, **438**, 168.
- 4 A. A. Balandin, S. Ghosh, W. Bao, I. Calizo, D. Teweldebrhan, F. Miao and C. N. Lau, *Nano Lett.*, 2008, **8**, 902–907.
- 5 H. Li, H. Ying, X. Chen, D. L. Nika, A. I. Cocemasov, W. Cai, A. A. Balandin and S. Chen, *Nanoscale*, 2014, **6**, 13402–13408.
- 6 C. Lee, X. Wei, J. W. Kysar and J. Hone, *Science*, 2008, **321**, 385–388.
- 7 I. Meric, M. Y. Han, A. F. Young, B. Ozyilmaz, P. Kim and K. L. Shepard, *Nat. Nanotechnol.*, 2008, **3**, 654–659.
- 8 S. Y. Zhou, G. H. Gweon, A. V. Fedorov, P. N. First, W. A. de Heer, D. H. Lee, F. Guinea, A. H. Castro Neto and A. Lanzara, *Nat. Mater.*, 2007, **6**, 770–775.
- 9 S. H. Cheng, K. Zou, F. Okino, H. R. Gutierrez, A. Gupta, N. Shen, P. C. Eklund, J. O. Sofo and J. Zhu, *Phys. Rev. B: Condens. Matter Mater. Phys.*, 2010, **81**, 205435.
- 10 R. Balog, B. Jorgensen, L. Nilsson, M. Andersen, E. Rienks, M. Bianchi, M. Fanetti, E. Laegsgaard, A. Baraldi, S. Lizzit, Z. Slijivancanin, F. Besenbacher, B. Hammer, T. G. Pedersen, P. Hofmann and L. Hornekaer, *Nat. Mater.*, 2010, **9**, 315–319.
- 11 L. Ci, L. Song, C. Jin, D. Jariwala, D. Wu, Y. Li, A. Srivastava, Z. F. Wang, K. Storr, L. Balicas, F. Liu and P. M. Ajayan, *Nat. Mater.*, 2010, **9**, 430–435.
- 12 L. Liu, J. Park, D. A. Siegel, K. F. McCarty, K. W. Clark, W. Deng, L. Basile, J. C. Idrobo, A. P. Li and G. Gu, *Science*, 2014, **343**, 163–167.
- 13 K. F. Mak, C. Lee, J. Hone, J. Shan and T. F. Heinz, *Phys. Rev. Lett.*, 2010, **105**, 136805.
- 14 L. Li, Y. Yu, G. J. Ye, Q. Ge, X. Ou, H. Wu, D. Feng, X. H. Chen and Y. Zhang, *Nat. Nanotechnol.*, 2014, **9**, 372–377.
- 15 R. Beams, L. G. Cancado, S. Krylyuk, I. Kalish, B. Kalanyan, A. K. Singh, K. Choudhary, A. Bruma, P. M. Vora, F. Tavazza, A. V. Davydov and S. J. Stranick, *ACS Nano*, 2016, **10**, 9626–9636.
- 16 A. V. Kolobov, P. Fons and J. Tominaga, *Phys. Rev. B: Condens. Matter Mater. Phys.*, 2016, **94**, 094114.
- 17 H. Zhang, C.-X. Liu, X.-L. Qi, X. Dai, Z. Fang and S.-C. Zhang, *Nat. Phys.*, 2009, **5**, 438–442.
- 18 Y. M. Lin, C. Dimitrakopoulos, K. A. Jenkins, D. B. Farmer, H. Y. Chiu, A. Grill and P. Avouris, *Science*, 2010, **327**, 662.
- 19 K. F. Mak, K. He, J. Shan and T. F. Heinz, *Nat. Nanotechnol.*, 2012, **7**, 494–498.
- 20 H. Zeng, J. Dai, W. Yao, D. Xiao and X. Cui, *Nat. Nanotechnol.*, 2012, **7**, 490–493.
- 21 T. Cao, G. Wang, W. Han, H. Ye, C. Zhu, J. Shi, Q. Niu, P. Tan, E. Wang, B. Liu and J. Feng, *Nat. Commun.*, 2012, **3**, 887.
- 22 V. Tran, R. Soklaski, Y. Liang and L. Yang, *Phys. Rev. B: Condens. Matter Mater. Phys.*, 2014, **89**, 235319.
- 23 J. Qiao, X. Kong, Z. X. Hu, F. Yang and W. Ji, *Nat. Commun.*, 2014, **5**, 4475.
- 24 F. Xia, H. Wang and Y. Jia, *Nat. Commun.*, 2014, **5**, 4458.
- 25 Q. Wei and X. Peng, *Appl. Phys. Lett.*, 2014, **104**, 251915.
- 26 S. Lan, S. Rodrigues, L. Kang and W. Cai, *ACS Photonics*, 2016, **3**, 1176–1181.
- 27 K. S. Novoselov, A. Mishchenko, A. Carvalho and A. H. Castro Neto, *Science*, 2016, **353**, aac9439.
- 28 A. K. Geim and I. V. Grigorieva, *Nature*, 2013, **499**, 419–425.
- 29 H. Li, J. B. Wu, F. Ran, M. L. Lin, X. L. Liu, Y. Zhao, X. Lu, Q. Xiong, J. Zhang, W. Huang, H. Zhang and P. H. Tan, *ACS Nano*, 2017, **11**, 11714–11723.
- 30 M. Baranowski, A. Surrente, L. Klopotoski, J. M. Urban, N. Zhang, D. K. Maude, K. Wiwatowski, S. Mackowski, Y. C. Kung, D. Dumcenco, A. Kis and P. Plochocka, *Nano Lett.*, 2017, **17**, 6360–6365.
- 31 F. W. K.-G. Zhou, Y. Cao, S. Hu, G. Yu and C. Casiraghi, *ACS Nano*, 2014, **8**, 9914–9924.
- 32 A. C. Ferrari and D. M. Basko, *Nat. Nanotechnol.*, 2013, **8**, 235–246.
- 33 L. M. Malard, M. A. Pimenta, G. Dresselhaus and M. S. Dresselhaus, *Phys. Rep.*, 2009, **473**, 51–87.
- 34 A. C. Ferrari, J. C. Meyer, V. Scardaci, C. Casiraghi, M. Lazzeri, F. Mauri, S. Piscanec, D. Jiang, K. S. Novoselov, S. Roth and A. K. Geim, *Phys. Rev. Lett.*, 2006, **97**, 187401.
- 35 A. Eckmann, A. Felten, A. Mishchenko, L. Britnell, R. Krupke, K. S. Novoselov and C. Casiraghi, *Nano Lett.*, 2012, **12**, 3925–3930.
- 36 L. G. Cancado, A. Jorio, E. H. Ferreira, F. Stavale, C. A. Achete, R. B. Capaz, M. V. Moutinho, A. Lombardo, T. S. Kulmala and A. C. Ferrari, *Nano Lett.*, 2011, **11**, 3190–3196.
- 37 A. Das, S. Pisana, B. Chakraborty, S. Piscanec, S. K. Saha, U. V. Waghmare, K. S. Novoselov, H. R. Krishnamurthy, A. K. Geim, A. C. Ferrari and A. K. Sood, *Nat. Nanotechnol.*, 2008, **3**, 210–215.
- 38 K. D. Park, M. B. Raschke, J. M. Atkin, Y. H. Lee and M. S. Jeong, *Adv. Mater.*, 2017, **29**, 1603601.
- 39 J.-B. Wu, M.-L. Lin, X. Cong, H.-N. Liu and P.-H. Tan, *Chem. Soc. Rev.*, 2018, **47**, 1822–1873.
- 40 X. Zhang, X. F. Qiao, W. Shi, J. B. Wu, D. S. Jiang and P. H. Tan, *Chem. Soc. Rev.*, 2015, **44**, 2757–2785.
- 41 X. Lu, X. Luo, J. Zhang, S. Y. Quek and Q. Xiong, *Nano Res.*, 2016, **9**, 3559–3597.
- 42 M. Born and K. Huang, *Dynamical theory of crystal lattices*, Clarendon press, 1954.
- 43 K. Golasa, M. Grzeszczyk, P. Leszczynski, C. Faugeras, A. A. L. Nicolet, A. Wyszczek, M. Potemski and A. Babinski, *Appl. Phys. Lett.*, 2014, **104**, 092106.
- 44 S. Gupta, E. Heintzman and J. Jasinski, *J. Raman Spectrosc.*, 2015, **46**, 217–230.
- 45 D. L. Mafra, G. Samsonidze, L. M. Malard, D. C. Elias, J. C. Brant, F. Plentz, E. S. Alves and M. A. Pimenta, *Phys. Rev. B: Condens. Matter Mater. Phys.*, 2007, **76**, 233407.
- 46 J. S. Park, A. Reina, R. Saito, J. Kong, G. Dresselhaus and M. S. Dresselhaus, *Carbon*, 2009, **47**, 1303–1310.
- 47 G. Wang, M. M. Glazov, C. Robert, T. Amand, X. Marie and B. Urbaszek, *Phys. Rev. Lett.*, 2015, **115**, 117401.
- 48 J. A. Wilson and A. D. Yoffe, *Adv. Phys.*, 1969, **18**, 193–334.
- 49 M. A. Pimenta, E. del Corro, B. R. Carvalho, C. Fantini and L. M. Malard, *Acc. Chem. Res.*, 2015, **48**, 41–47.
- 50 M. Topsakal, E. Aktürk and S. Ciraci, *Phys. Rev. B: Condens. Matter Mater. Phys.*, 2009, **79**, 115442.

- 51 A. Molina-Sanchez and L. Wirtz, *Phys. Rev. B: Condens. Matter Mater. Phys.*, 2011, **84**, 155413.
- 52 Q. Cai, D. Scullion, A. Falin, K. Watanabe, T. Taniguchi, Y. Chen, E. J. Santos and L. H. Li, *Nanoscale*, 2017, **9**, 3059–3067.
- 53 H. Terrones, E. Del Corro, S. Feng, J. M. Poumirol, D. Rhodes, D. Smirnov, N. R. Pradhan, Z. Lin, M. A. T. Nguyen, A. L. Elias, T. E. Mallouk, L. Balicas, M. A. Pimenta and M. Terrones, *Sci. Rep.*, 2014, **4**, 4215.
- 54 Y. Feng, W. Zhou, Y. Wang, J. Zhou, E. Liu, Y. Fu, Z. Ni, X. Wu, H. Yuan, F. Miao, B. Wang, X. Wan and D. Xing, *Phys. Rev. B: Condens. Matter Mater. Phys.*, 2015, **92**, 054110.
- 55 A. M. Stacy and D. T. Hodul, *J. Phys. Chem. Solids*, 1985, **46**, 405–409.
- 56 L. Sun, J. Yan, D. Zhan, L. Liu, H. Hu, H. Li, B. K. Tay, J.-L. Kuo, C.-C. Huang, D. W. Hewak, P. S. Lee and Z. X. Shen, *Phys. Rev. Lett.*, 2013, **111**, 126801.
- 57 W. Kohn, *Phys. Rev. Lett.*, 1959, **2**, 393–394.
- 58 S. Piscanec, M. Lazzeri, F. Mauri, A. C. Ferrari and J. Robertson, *Phys. Rev. Lett.*, 2004, **93**, 185503.
- 59 A. McCreary, J. R. Simpson, Y. Wang, D. Rhodes, K. Fujisawa, L. Balicas, M. Dubey, V. H. Crespi, M. Terrones and A. R. H. Walker, *Nano Lett.*, 2017, **17**, 5897–5907.
- 60 S. Dong, A. Zhang, K. Liu, J. Ji, Y. G. Ye, X. G. Luo, X. H. Chen, X. Ma, Y. Jie, C. Chen, X. Wang and Q. Zhang, *Phys. Rev. Lett.*, 2016, **116**, 087401.
- 61 X. Ling, L. Liang, S. Huang, A. A. Puzos, D. B. Geohegan, B. G. Sumpter, J. Kong, V. Meunier and M. S. Dresselhaus, *Nano Lett.*, 2015, **15**, 4080–4088.
- 62 E. Lorchat, G. Froehlicher and S. Berciaud, *ACS Nano*, 2016, **10**, 2752–2760.
- 63 X. Ling, S. Huang, E. H. Hasdeo, L. Liang, W. M. Parkin, Y. Tatsumi, A. R. Nugraha, A. A. Puzos, P. M. Das, B. G. Sumpter, D. B. Geohegan, J. Kong, R. Saito, M. Drndic, V. Meunier and M. S. Dresselhaus, *Nano Lett.*, 2016, **16**, 2260–2267.
- 64 D. Tan, H. E. Lim, F. Wang, N. B. Mohamed, S. Mouri, W. Zhang, Y. Miyauchi, M. Ohfuchi and K. Matsuda, *Nano Res.*, 2016, **10**, 546–555.
- 65 J. He, D. He, Y. Wang, Q. Cui, M. Z. Bellus, H. Y. Chiu and H. Zhao, *ACS Nano*, 2015, **9**, 6436.
- 66 R. Fei and L. Yang, *Nano Lett.*, 2014, **14**, 2884.
- 67 W. Kong, C. Bacaksiz, B. Chen, K. Wu, M. Blei, X. Fan, Y. Shen, H. Sahin, D. Wright, D. S. Narang and S. Tongay, *Nanoscale*, 2017, **9**, 4175–4182.
- 68 J. Wu, N. Mao, L. Xie, H. Xu and J. Zhang, *Angew. Chem., Int. Ed.*, 2015, **54**, 2366–2369.
- 69 N. Mao, J. Wu, B. Han, J. Lin, L. Tong and J. Zhang, *Small*, 2016, **12**, 2627–2633.
- 70 J. Lin, L. Liang, X. Ling, S. Zhang, N. Mao, N. Zhang, B. G. Sumpter, V. Meunier, L. Tong and J. Zhang, *J. Am. Chem. Soc.*, 2015, **137**, 15511–15517.
- 71 D. A. Chenet, O. B. Aslan, P. Y. Huang, C. Fan, A. M. van der Zande, T. F. Heinz and J. C. Hone, *Nano Lett.*, 2015, **15**, 5667–5672.
- 72 A. L. Phaneuf-L'Heureux, A. Favron, J. F. Germain, P. Lavoie, P. Desjardins, R. Leonelli, R. Martel and S. Francoeur, *Nano Lett.*, 2016, **16**, 7761–7767.
- 73 R. Loudon, *Adv. Phys.*, 2001, **50**, 813–864.
- 74 L. Liang and V. Meunier, *Nanoscale*, 2014, **6**, 5394–5401.
- 75 X. Zhang, W. P. Han, J. B. Wu, S. Milana, Y. Lu, Q. Q. Li, A. C. Ferrari and P. H. Tan, *Phys. Rev. B: Condens. Matter Mater. Phys.*, 2013, **87**, 115413.
- 76 J. Kim, J. U. Lee, J. Lee, H. J. Park, Z. Lee, C. Lee and H. Cheong, *Nanoscale*, 2015, **7**, 18708–18715.
- 77 H. B. Ribeiro, M. A. Pimenta, C. J. S. de Matos, R. L. Moreira, A. S. Rodin, J. D. Zapata, E. A. T. de Souza and A. H. Castro Neto, *ACS Nano*, 2015, **9**, 4270–4276.
- 78 Z. Tian, C. Guo, M. Zhao, R. Li and J. Xue, *ACS Nano*, 2017, **11**, 2219–2226.
- 79 S. Luo, X. Qi, H. Yao, X. Ren, Q. Chen and J. Zhong, *J. Phys. Chem. C*, 2017, **121**, 4674–4679.
- 80 X. Wang, Y. Li, L. Huang, X.-W. Jiang, L. Jiang, H. Dong, Z. Wei, J. Li and W. Hu, *J. Am. Chem. Soc.*, 2017, **139**, 14976–14982.
- 81 S. Zhang, N. Mao, N. Zhang, J. Wu, L. Tong and J. Zhang, *ACS Nano*, 2017, **11**, 10366–10372.
- 82 L. Hart, S. Dale, S. Hoyer, J. L. Webb and D. Wolverson, *Nano Lett.*, 2016, **16**, 1381–1386.
- 83 S. Huang, Y. Tatsumi, X. Ling, H. Guo, Z. Wang, G. Watson, A. A. Puzos, D. B. Geohegan, J. Kong, J. Li, T. Yang, R. Saito and M. S. Dresselhaus, *ACS Nano*, 2016, **10**, 8964–8972.
- 84 M. S. Dresselhaus, A. Jorio, A. G. Souza Filho and R. Saito, *Philos. Trans. R. Soc., A*, 2010, **368**, 5355–5377.
- 85 L. Gustavo Cançado, M. Gomes da Silva, E. H. Martins Ferreira, F. Hof, K. Kampioti, K. Huang, A. Pénicaud, C. Alberto Achete, R. B. Capaz and A. Jorio, *2D Mater.*, 2017, **4**, 025039.
- 86 M. A. Pimenta, G. Dresselhaus, M. S. Dresselhaus, L. G. Cancado, A. Jorio and R. Saito, *Phys. Chem. Chem. Phys.*, 2007, **9**, 1276–1291.
- 87 J.-U. Lee, M. Kim and H. Cheong, *Appl. Microsc.*, 2015, **45**, 126–130.
- 88 R. Saito, A. Jorio, A. G. Souza Filho, G. Dresselhaus, M. S. Dresselhaus and M. A. Pimenta, *Phys. Rev. Lett.*, 2002, **88**, 027401.
- 89 N. T. McDevitt, J. S. Zabinski, M. S. Donley and J. E. Bultman, *Appl. Spectrosc.*, 1994, **48**, 733–736.
- 90 G. L. Frey, R. Tenne, M. J. Matthews, M. S. Dresselhaus and G. Dresselhaus, *J. Mater. Res.*, 2011, **13**, 2412–2417.
- 91 S. Mignuzzi, A. J. Pollard, N. Bonini, B. Brennan, I. S. Gilmore, M. A. Pimenta, D. Richards and D. Roy, *Phys. Rev. B: Condens. Matter Mater. Phys.*, 2015, **91**, 195411.
- 92 E. H. Martins Ferreira, M. V. O. Moutinho, F. Stavale, M. M. Lucchese, R. B. Capaz, C. A. Achete and A. Jorio, *Phys. Rev. B: Condens. Matter Mater. Phys.*, 2010, **82**, 125429.
- 93 E. del Corro, H. Terrones, A. Elias, C. Fantini, S. Feng, M. A. Nguyen, T. E. Mallouk, M. Terrones and M. A. Pimenta, *ACS Nano*, 2014, **8**, 9629–9635.
- 94 M. Mahjouri-Samani, L. Liang, A. Oyedele, Y. S. Kim, M. Tian, N. Cross, K. Wang, M. W. Lin, A. Boulesbaa, C. M. Rouleau, A. A. Puzos, K. Xiao, M. Yoon, G. Eres, G. Duscher, B. G. Sumpter and D. B. Geohegan, *Nano Lett.*, 2016, **16**, 5213–5220.
- 95 F. Tuinstra and J. L. Koenig, *J. Chem. Phys.*, 1970, **53**, 1126–1130.

- 96 M. M. Lucchese, F. Stavale, E. H. M. Ferreira, C. Vilani, M. V. O. Moutinho, R. B. Capaz, C. A. Achete and A. Jorio, *Carbon*, 2010, **48**, 1592–1597.
- 97 K. Nakada, M. Fujita, G. Dresselhaus and M. S. Dresselhaus, *Phys. Rev. B: Condens. Matter Mater. Phys.*, 1996, **54**, 17954–17961.
- 98 Y. You, Z. Ni, T. Yu and Z. Shen, *Appl. Phys. Lett.*, 2008, **93**, 163112.
- 99 L. G. Cancado, M. A. Pimenta, B. R. Neves, M. S. Dantas and A. Jorio, *Phys. Rev. Lett.*, 2004, **93**, 247401.
- 100 C. Casiraghi, A. Hartschuh, H. Qian, S. Piscanec, C. Georgi, A. Fasoli, K. S. Novoselov, D. M. Basko and A. C. Ferrari, *Nano Lett.*, 2009, **9**, 1433–1441.
- 101 H. B. Ribeiro, C. E. Villegas, D. A. Bahamon, D. Muraca, A. H. Castro Neto, E. A. de Souza, A. R. Rocha, M. A. Pimenta and C. J. de Matos, *Nat. Commun.*, 2016, **7**, 12191.
- 102 L. Zhao, R. He, K. T. Rim, T. Schiros, K. S. Kim, H. Zhou, C. Gutiérrez, S. P. Chockalingam, C. J. Arguello, L. Pálková, D. Nordlund, M. S. Hybertsen, D. R. Reichman, T. F. Heinz, P. Kim, A. Pinczuk, G. W. Flynn and A. N. Pasupathy, *Science*, 2011, **333**, 999–1003.
- 103 Y.-C. Lin, C.-Y. Lin and P.-W. Chiu, *Appl. Phys. Lett.*, 2010, **96**, 133110.
- 104 J. Yan, Y. Zhang, P. Kim and A. Pinczuk, *Phys. Rev. Lett.*, 2007, **98**, 166802.
- 105 R. Voggu, B. Das, C. S. Rout and C. N. R. Rao, *J. Phys.: Condens. Matter*, 2008, **20**, 472204.
- 106 J. Sun, J. Qian, M. Zhai, F. Liu, C. Qi, X. Shi, G. Wang, R. Xiong and S. Ye, *Chem. Phys. Lett.*, 2015, **638**, 47–51.
- 107 B. Chakraborty, A. Bera, D. V. S. Muthu, S. Bhowmick, U. V. Waghmare and A. K. Sood, *Phys. Rev. B: Condens. Matter Mater. Phys.*, 2012, **85**, 161403.
- 108 M. Yamamoto, T. L. Einstein, M. S. Fuhrer and W. G. Cullen, *J. Phys. Chem. C*, 2013, **117**, 25643–25649.
- 109 Y. Gong, S. Lei, G. Ye, B. Li, Y. He, K. Keyshar, X. Zhang, Q. Wang, J. Lou, Z. Liu, R. Vajtai, W. Zhou and P. M. Ajayan, *Nano Lett.*, 2015, **15**, 6135–6141.
- 110 M. H. Doan, Y. Jin, S. Adhikari, S. Lee, J. Zhao, S. C. Lim and Y. H. Lee, *ACS Nano*, 2017, **11**, 3832–3840.
- 111 M. S. Choi, G. H. Lee, Y. J. Yu, D. Y. Lee, S. H. Lee, P. Kim, J. Hone and W. J. Yoo, *Nat. Commun.*, 2013, **4**, 1624.
- 112 M. L. Tsai, M. Y. Li, J. R. D. Retamal, K. T. Lam, Y. C. Lin, K. Suenaga, L. J. Chen, G. Liang, L. J. Li and J. H. He, *Adv. Mater.*, 2017, **29**, 1701168.
- 113 M. Mahjouri-Samani, M. W. Lin, K. Wang, A. R. Lupini, J. Lee, L. Basile, A. Boulesbaa, C. M. Rouleau, A. A. Puzos, I. N. Ivanov, K. Xiao, M. Yoon and D. B. Geohegan, *Nat. Commun.*, 2015, **6**, 7749.
- 114 K. Liu, L. Zhang, T. Cao, C. Jin, D. Qiu, Q. Zhou, A. Zettl, P. Yang, S. G. Louie and F. Wang, *Nat. Commun.*, 2014, **5**, 4966.
- 115 X. F. Qiao, J. B. Wu, L. Zhou, J. Qiao, W. Shi, T. Chen, X. Zhang, J. Zhang, W. Ji and P. H. Tan, *Nanoscale*, 2016, **8**, 8324–8332.
- 116 M. Koshino, *Phys. Rev. B: Condens. Matter Mater. Phys.*, 2010, **81**, 125304.
- 117 S. X. Huang, L. B. Liang, X. Ling, A. A. Puzos, D. B. Geohegan, B. G. Sumpter, J. Kong, V. Meunier and M. S. Dresselhaus, *Nano Lett.*, 2016, **16**, 1435–1444.
- 118 M. Zhao, W. Zhang, M. Liu, C. Zou, K. Yang, Y. Yang, Y. Dong, L. Zhang and S. Huang, *Nano Res.*, 2016, **9**, 3772–3780.
- 119 S. Latil and L. Henrard, *Phys. Rev. Lett.*, 2006, **97**, 036803.
- 120 M. Otani, M. Koshino, Y. Takagi and S. Okada, *Phys. Rev. B: Condens. Matter Mater. Phys.*, 2010, **81**, 161403.
- 121 E. McCann and M. Koshino, *Phys. Rev. B: Condens. Matter Mater. Phys.*, 2010, **81**, 241409.
- 122 C. H. Lui, Z. Li, Z. Chen, P. V. Klimov, L. E. Brus and T. F. Heinz, *Nano Lett.*, 2011, **11**, 164–169.
- 123 T. A. Nguyen, J. U. Lee, D. Yoon and H. Cheong, *Sci. Rep.*, 2014, **4**, 4630.
- 124 L. M. Malard, M. H. D. Guimarães, D. L. Mafra, M. S. C. Mazzoni and A. Jorio, *Phys. Rev. B: Condens. Matter Mater. Phys.*, 2009, **79**.
- 125 C. Cong, T. Yu, K. Sato, J. Shang, R. Saito, G. F. Dresselhaus and M. S. Dresselhaus, *ACS Nano*, 2011, **5**, 8760–8768.
- 126 C. H. Lui, Z. Ye, C. Keiser, E. B. Barros and R. He, *Appl. Phys. Lett.*, 2015, **106**, 041904.
- 127 K. S. Novoselov, E. McCann, S. V. Morozov, V. I. Fal'ko, M. I. Katsnelson, U. Zeitler, D. Jiang, F. Schedin and A. K. Geim, *Nat. Phys.*, 2006, **2**, 177–180.
- 128 T. Ohta, A. Bostwick, T. Seyller, K. Horn and E. Rotenberg, *Science*, 2006, **313**, 951–954.
- 129 J. B. Oostinga, H. B. Heersche, X. Liu, A. F. Morpurgo and L. M. Vandersypen, *Nat. Mater.*, 2008, **7**, 151–157.
- 130 Z. F. Wang, F. Liu and M. Y. Chou, *Nano Lett.*, 2012, **12**, 3833–3838.
- 131 A. Luican, G. Li, A. Reina, J. Kong, R. R. Nair, K. S. Novoselov, A. K. Geim and E. Y. Andrei, *Phys. Rev. Lett.*, 2011, **106**, 126802.
- 132 R. He, T.-F. Chung, C. Delaney, C. Keiser, L. A. Jauregui, P. M. Shand, C. C. Chancey, Y. Wang, J. Bao and Y. P. Chen, *Nano Lett.*, 2013, **13**, 3594–3601.
- 133 P. Ramnani, M. R. Neupane, S. Ge, A. A. Balandin, R. K. Lake and A. Mulchandani, *Carbon*, 2017, **123**, 302–306.
- 134 K. Kim, S. Coh, L. Z. Tan, W. Regan, J. M. Yuk, E. Chatterjee, M. F. Crommie, M. L. Cohen, S. G. Louie and A. Zettl, *Phys. Rev. Lett.*, 2012, **108**, 246103.
- 135 W. Yan, M. Liu, R. F. Dou, L. Meng, L. Feng, Z. D. Chu, Y. Zhang, Z. Liu, J. C. Nie and L. He, *Phys. Rev. Lett.*, 2012, **109**, 126801.
- 136 A. K. Gupta, Y. Tang, V. H. Crespi and P. C. Eklund, *Phys. Rev. B: Condens. Matter Mater. Phys.*, 2010, **82**, 241406.
- 137 V. Carozo, C. M. Almeida, E. H. Ferreira, L. G. Cancado, C. A. Achete and A. Jorio, *Nano Lett.*, 2011, **11**, 4527–4534.
- 138 A. N. Grigorenko, M. Polini and K. S. Novoselov, *Nat. Photonics*, 2012, **6**, 749–758.
- 139 J. B. Wu, X. Zhang, M. Ijas, W. P. Han, X. F. Qiao, X. L. Li, D. S. Jiang, A. C. Ferrari and P. H. Tan, *Nat. Commun.*, 2014, **5**, 5309.
- 140 J. U. Lee, K. Kim, S. Han, G. H. Ryu, Z. Lee and H. Cheong, *ACS Nano*, 2016, **10**, 1948–1953.
- 141 J. Yan, J. Xia, X. Wang, L. Liu, J. L. Kuo, B. K. Tay, S. Chen, W. Zhou, Z. Liu and Z. X. Shen, *Nano Lett.*, 2015, **15**, 8155–8161.

- 142 A. A. Puzos, L. Liang, X. Li, K. Xiao, K. Wang, M. Mahjouri-Samani, L. Basile, J. C. Idrobo, B. G. Sumpter, V. Meunier and D. B. Geohegan, *ACS Nano*, 2015, **9**, 6333–6342.
- 143 X. Lu, M. I. Utama, J. Lin, X. Luo, Y. Zhao, J. Zhang, S. T. Pantelides, W. Zhou, S. Y. Quek and Q. Xiong, *Adv. Mater.*, 2015, **27**, 4502–4508.
- 144 S. Zheng, L. Sun, X. Zhou, F. Liu, Z. Liu, Z. Shen and H. J. Fan, *Adv. Opt. Mater.*, 2015, **3**, 1600–1605.
- 145 S. Huang, X. Ling, L. Liang, J. Kong, H. Terrones, V. Meunier and M. S. Dresselhaus, *Nano Lett.*, 2014, **14**, 5500–5508.
- 146 V. Senthilkumar, L. C. Tam, Y. S. Kim, Y. Sim, M.-J. Seong and J. I. Jang, *Nano Res.*, 2014, **7**, 1759–1768.
- 147 J. W. Jiang, B. S. Wang and H. S. Park, *J. Phys.: Condens. Matter*, 2016, **28**, 165401.
- 148 X. Luo, X. Lu, G. K. Koon, A. H. Castro Neto, B. Ozyilmaz, Q. Xiong and S. Y. Quek, *Nano Lett.*, 2015, **15**, 3931–3938.
- 149 H. L. Kang, H. J. Shin, J. Lee, I. Lee, G. H. Kim, J. Y. Choi and S. W. Kim, *Nano Lett.*, 2012, **12**, 714–718.
- 150 C. Ojedaaristizabal, S. Ejg, S. Onishi, A. Yan, H. I. Rasool, S. Kahn, Y. Lv, D. Latzke, J. Velasco Jr and M. F. Crommie, *ACS Nano*, 2017, **11**, 4686–4693.
- 151 A. Eckmann, J. Park, H. Yang, D. Elias, A. S. Mayorov, G. Yu, R. Jalil, K. S. Novoselov, R. V. Gorbachev and M. Lazzeri, *Nano Lett.*, 2013, **13**, 5242.
- 152 S. Wang, X. Wang and J. H. Warner, *ACS Nano*, 2015, **9**, 5246.
- 153 C. H. Lui, Z. P. Ye, C. Ji, K. C. Chiu, C. T. Chou, T. I. Andersen, C. Means-Shively, H. Anderson, J. M. Wu, T. Kidd, Y. H. Lee and R. He, *Phys. Rev. B: Condens. Matter Mater. Phys.*, 2015, **91**, 165403.
- 154 K. Wang, B. Huang, M. Tian, F. Ceballos, M. W. Lin, M. Mahjouri-Samani, A. Boulesbaa, A. A. Puzos, C. M. Rouleau, M. Yoon, H. Zhao, K. Xiao, G. Duscher and D. B. Geohegan, *ACS Nano*, 2016, **10**, 6612–6622.
- 155 J. Stadler, T. Schmid and R. Zenobi, *ACS Nano*, 2011, **5**, 8442–8448.
- 156 S. Mignuzzi, N. Kumar, B. Brennan, I. S. Gilmore, D. Richards, A. J. Pollard and D. Roy, *Nanoscale*, 2015, **7**, 19413–19418.
- 157 M. Liao, S. Jiang, C. Hu, R. Zhang, Y. Kuang, J. Zhu, Y. Zhang and Z. Dong, *Nano Lett.*, 2016, **16**, 4040–4046.
- 158 R. Beams, L. G. Cancado, A. Jorio, A. N. Vamivakas and L. Novotny, *Nanotechnology*, 2015, **26**, 175702.
- 159 K. D. Park, O. Khatib, V. Kravtsov, G. Clark, X. Xu and M. B. Raschke, *Nano Lett.*, 2016, **16**, 2621–2627.
- 160 M. Ghislandi, G. G. Hoffmann, E. Tkalya, L. Xue and G. D. With, *Appl. Spectrosc. Rev.*, 2012, **47**, 371–381.
- 161 S. Coh, L. Z. Tan, S. G. Louie and M. L. Cohen, *Phys. Rev. B: Condens. Matter Mater. Phys.*, 2013, **88**, 165431.
- 162 D. Jose, A. Nijamudheen and A. Datta, *Phys. Chem. Chem. Phys.*, 2013, **15**, 8700–8704.
- 163 J.-H. Zhong, X. Jin, L. Meng, X. Wang, H.-S. Su, Z.-L. Yang, C. T. Williams and B. Ren, *Nat. Nanotechnol.*, 2016, **12**, 132.
- 164 M. Rahaman, R. D. Rodriguez, G. Plechinger, S. Moras, C. Schüller, T. Korn and D. R. T. Zahn, *Nano Lett.*, 2017, **17**, 6027–6033.
- 165 P. Ajayan, P. Kim and K. Banerjee, *Phys. Today*, 2016, **69**, 39–44.
- 166 D. Jariwala, T. J. Marks and M. C. Hersam, *Nat. Mater.*, 2017, **16**, 170–181.
- 167 Y. J. Zheng, Y. L. Huang, Y. Chen, W. Zhao, G. Eda, C. D. Spataru, W. Zhang, Y.-H. Chang, L.-J. Li and D. Chi, *ACS Nano*, 2016, **10**, 2476–2484.
- 168 A. Campion and P. Kambhampati, *Chem. Soc. Rev.*, 1998, **27**, 241–250.
- 169 Y. Tan, L. Ma, Z. Gao, M. Chen and F. Chen, *Nano Lett.*, 2017, **17**, 2621–2626.
- 170 W. Xu, N. Mao and J. Zhang, *Small*, 2013, **9**, 1206–1224.
- 171 V. R. Dantham, P. B. Bisht, B. S. Kalanoor, T. T. Baby and S. Ramaprabhu, *Chem. Phys. Lett.*, 2012, **521**, 130–133.
- 172 B. Das, R. Voggu, C. S. Rout and C. N. R. Rao, *Chem. Commun.*, 2008, 5155–5157, DOI: 10.1039/b808955h.
- 173 N. Jung, N. Kim, S. Jockusch, N. J. Turro, P. Kim and L. Brus, *Nano Lett.*, 2009, **9**, 4133–4137.
- 174 Y. H. Lu, W. Chen, Y. P. Feng and P. M. He, *J. Phys. Chem. B*, 2009, **113**, 2–5.
- 175 A. K. Manna and S. K. Pati, *Chem. – Asian J.*, 2009, **4**, 855–860.
- 176 H. Pinto, R. Jones, J. P. Goss and P. R. Briddon, *J. Phys.: Condens. Matter*, 2009, **21**, 402001.
- 177 S. K. Saha, R. C. Chandrakanth, H. R. Krishnamurthy and U. V. Waghmare, *Phys. Rev. B: Condens. Matter Mater. Phys.*, 2009, **80**, 155414.
- 178 J. T. Sun, Y. H. Lu, W. Chen, Y. P. Feng and A. T. S. Wee, *Phys. Rev. B: Condens. Matter Mater. Phys.*, 2010, **81**, 155403.
- 179 L. Xie, X. Ling, Y. Fang, J. Zhang and Z. Liu, *J. Am. Chem. Soc.*, 2009, **131**, 9890–9891.
- 180 X. Ling, L. Xie, Y. Fang, H. Xu, H. Zhang, J. Kong, M. S. Dresselhaus, J. Zhang and Z. Liu, *Nano Lett.*, 2010, **10**, 553–561.
- 181 X. Ling and J. Zhang, *Acta Phys.-Chim. Sin.*, 2012, **28**, 2355–2362.
- 182 X. Ling and J. Zhang, *Small*, 2010, **6**, 2020–2025.
- 183 H. Xu, Y. Chen, W. Xu, H. Zhang, J. Kong, M. S. Dresselhaus and J. Zhang, *Small*, 2011, **7**, 2945–2952.
- 184 H. Xu, L. Xie, H. Zhang and J. Zhang, *ACS Nano*, 2011, **5**, 5338–5344.
- 185 X. Ling, J. Wu, W. Xu and J. Zhang, *Small*, 2012, **8**, 1365–1372.
- 186 S. Huang, X. Ling, L. Liang, Y. Song, W. Fang, J. Zhang, J. Kong, V. Meunier and M. S. Dresselhaus, *Nano Lett.*, 2015, **15**, 2892–2901.
- 187 E. B. Barros and M. S. Dresselhaus, *Phys. Rev. B: Condens. Matter Mater. Phys.*, 2014, **90**, 035443.
- 188 Y. Joo, M. Kim, C. Kanimozhi, P. Huang, B. M. Wong, S. S. Roy, M. S. Arnold and P. Gopalan, *J. Phys. Chem. C*, 2016, **120**, 13815–13824.
- 189 X. Ling, W. Fang, Y.-H. Lee, P. T. Araujo, X. Zhang, J. F. Rodriguez-Nieva, Y. Lin, J. Zhang, J. Kong and M. S. Dresselhaus, *Nano Lett.*, 2014, **14**, 3033–3040.
- 190 X. Wang, A. M. Jones, K. L. Seyler, V. Tran, Y. Jia, H. Zhao, H. Wang, L. Yang, X. Xu and F. Xia, *Nat. Nanotechnol.*, 2015, **10**, 517.
- 191 E. Liu, Y. Fu, Y. Wang, Y. Feng, H. Liu, X. Wan, W. Zhou, B. Wang, L. Shao and C. H. Ho, *Nat. Commun.*, 2015, **6**, 6991.
- 192 T. Yang, L. Ma, Z. Gao, C. Ming and C. Feng, *Nano Lett.*, 2017, **17**, 2621–2626.